Measurement of the Top Quark Pair Production Cross Section and an in-situ B-tagging efficiency Calibration with ATLAS in pp collisions at $\sqrt{s} = 7$ TeV in Dilepton Final States

by

Bin Guo

A thesis submitted in conformity with the requirements
for the degree of Doctor of Philosophy
Graduate Department of Physics
University of Toronto

Abstract

Measurement of the Top Quark Pair Production Cross Section and an in-situ B-tagging efficiency Calibration with ATLAS in pp collisions at $\sqrt{s} = 7$ TeV in Dilepton Final States

Bin Guo

Doctor of Philosophy

Graduate Department of Physics

University of Toronto

2011

We present a measurement of the top anti-top quark ($t\bar{t}$) production cross section in the dilepton final states from proton-proton collisions at a center of mass energy at 7 TeV at the LHC. A b-tagging algorithm based on tracks displaced from the event interaction vertex is applied to identify bottom quark jets from top quark decay and reject background events. Given the relatively pure sample of bottom quark jets in $t\bar{t}$ dilepton final states, a new technique to measure in-situ the b-tagging efficiency is introduced that uses the distribution of the number of observed b-tagged jets. We present results with data collected at the ATLAS detector in 2010 with an integrated luminosity of 35 pb^{-1}. The measured $t\bar{t}$ cross section is $176^{+22}_{-21}(\text{stat.})^{+20}_{-20}(\text{syst.}) \pm 6(\text{lum.})$ pb in the dilepton channel. We will also discuss the future prospects of this measurement.

Acknowledgements

Looking back, I am very grateful for all I have received. The achievements, the gratifications, as well as the struggles have shaped my character and led me where I am now. All these years of my graduate studies are full of such gifts.

There are no words can express my gratitude to my Ph.D. supervisor, Professor Pekka Sinervo. Pekka's supervision, ideas, support, encouragement, and patience made my graduate degree possible. Moreover, the example Pekka is as a person has become my lifelong treasure. I feel privileged and it is my honor to become Pekka's first ATLAS student.

I had great experience working with the ATLAS group in Toronto. I still remember when I first traveled to CERN in the summer of 2006, Prof. Richard Teuscher helped me start my very first ATLAS project. Since then, I received continuous support and guidance from Richard and all the members of the ATLAS Toronto group during my Ph.D. studies. I would like to thank Prof. Peter Krieger, Prof. Pierre Savard, Prof. William Trischuk and Prof. Bob Orr for the help and advice in many aspects of my student life. I enjoyed very much working with the research associates in our group: Dr. Rachid Mazini, Dr. Lianliang Ma, Dr. Adam Gibson, Dr. Neil Knecht, Dr. Bertrand Brelier and Dr. Teresa Spreitzer. I am grateful to my Ph.D. committee members Prof. John Martin and Prof. Erich Poppitz. I would like to thank Dr. Leslie Groer, Greg Wu and Krystyna Biel for all their support.

It was great fortune to be accompanied by my colleagues and friends Sing, Pier-Olivier, Dominique, Trevor, Gabe, Saminder, Behi, Peter, Cristen, Travis, and Trisha. The discussions with them were always sources of good ideas toward my questions. I will miss the good times we spent together in our Ph.D.'s in Toronto.

I am obliged to many people in the ATLAS collaboration, specifically people in the top and b-tagging groups. In particular I would like to thank Dr. Chuanlei Liu. Without the combined effort from the collaboration, my analysis would never have been possible.

Contents

List of Tables

List of Figures

Chapter 1

Introduction

The field of physics attempts to understand the complexities of nature and the physical phenomena that are observed. In particular, particle physics seeks to understand the constituents of the universe and their interactions. Over the last century, we developed a theory called the Standard Model (SM) [1, 2, 3] of particle physics to explain such physical phenomena. For the past several decades, high energy accelerators and colliders have been our primary experimental tools for particle physics. The Large Hadron Collider (LHC) at CERN, currently the most energetic particle collider, has completed its first year of operation. This starts a new era where we will be exploring the physics beyond the SM and fully testing the existing theories.

The observation and the studies of top quark pair production is one of the key milestones for the LHC program for several reasons. First of all, the early stage of the physics program will be important for the commissioning of the detector and its computing support. Thanks to the complex topology of their decays, most of the subdetectors of which ATLAS is composed must be fully operational. The abundant sample of $t\bar{t}$ events is well suited for use as a calibration tool for reconstructed leptons, jets and b-quark tagging algorithms. Furthermore, $t\bar{t}$ events are important backgrounds in the searches for the Higgs boson or physics beyond the Standard Model and it is therefore crucial to under-

stand this process in detail. Finally, uncertainties on the theoretical predictions for the $t\bar{t}$ pair production cross section are now at the level of 10% [4] and a comparison with experimental measurements will allow for a test of the expectations from the SM and possible new production mechanisms beyond the SM.

The identification of jets originating from b-quarks is an important part of the LHC physics program, in precision measurements to test the SM as well as in the search for new phenomena [5]. At the beginning of LHC data taking, the performance of the b-tagging algorithms has to be understood using data. At the LHC, the large $t\bar{t}$ production cross section, the relative low background rates, and the high b-jet purity make the $t\bar{t}$ sample useful to determine the b-tagging efficiency.

This thesis presents a measurement of the $t\bar{t}$ production cross section in proton-proton collisions at a center of mass energy of 7 TeV using data produced by the LHC and recorded by the ATLAS detector. The b-tagging efficiency is also measured simultaneously using the distribution of number of observed b-tagged jets. The outline of this thesis is as follows: Chapter 2 reviews the theoretical aspects of top quarks, their production mechanism, decay channels and properties. Chapter 3 outlines the ATLAS experiment at the LHC, including a brief summary of the LHC and a detailed description of the ATLAS detector. Chapter 4 describes the data sample and event selection criteria that was used in this thesis. Chapter 5 summarizes the expected background and observed event yields using these selection criteria. Chapter 6 provides an introduction to the b-quark jets identification algorithms. Chapters 7 and 8 present a new technique to simultaneously measure the $t\bar{t}$ production cross section and the efficiency of identifying b-quark jets. Finally, the results and conclusions using this technique are summarized in Chapter 9.

Chapter 2

Theoretical Context

2.1 The Standard Model of Particle Physics

The standard model of particle physics is a theory concerning the known subatomic particles. It was developed throughout the middle to late 20th century, and the current formulation was finalized in the mid-1970s upon the development of electroweak unification theory and the framework to accommodate three quark and lepton generations [1, 2, 3].

2.1.1 Quarks and Leptons

Just as the existence of three particles, the neutron, proton, and electron, explained the existence of about 100 types of atoms, sub-components of neutrons and protons, named quarks, have been hypothesized to explain the varieties of observed particles in high-energy experiments in the second half of the 20th century[6, 7]. Under the quark model, only three type of quarks (up, down and strange) were required to explain hundreds of particles observed at the time. More quarks were proposed and discovered later on. In 1974, scientists at SLAC [8] and Brookhaven [9] discovered the J/Ψ meson, which proved to be constituted of a quark/anti-quark pair of a "new" quark, now called charm(c). In 1977, a new meson was discovered at Fermilab, very similar to the J/Ψ

but much more massive, called the upsilon (Υ), and confirmed the existence of a new flavor of quarks, called beauty or bottom (b) [10]. A sixth quark, the top quark, was also predicted to explain observed CP violations in kaon decay [11] and the measured $b\bar{b}$ angular distribution. The first observations of the top quark were reported by the CDF [12] and D0 [13] collaborations in 1995. The unique properties of the top quark separate itself from all other quarks and make itself an interesting object to study.

A second family of particles, known as leptons, complete the fundamental building blocks of matter in the SM. The most familiar one is the electron, discovered in 1897 by J.J.Thomson. In 1936, the muon was discovered and later confirmed to have the same properties as the electron except for being about 200 times more massive. In 1977, a third lepton, called the tau (τ), with mass of about 1.8 GeV, was discovered at SLAC [14]. Besides these charged leptons, three different neutral leptons, neutrinos, also exist. The neutrino was first hypothesized to explain the energy spectrum in beta decay, in which a beta particle (an electron or a positron) is emitted. If only an electron is emitted in the decay process, its energy spectrum is expected to be discrete due to conservation of energy and momentum. However, the observed energy spectrum of the electron is continuous rather than discrete. Wolfgang Pauli and Enrico Fermi suggested that a very light and neutral particle is produced but not detected in the decay, which carries away energy and momentum and explains the observed spectrum. The existences of neutrinos was later directly confirmed experimentally in 1956 [15]. It was also demonstrated that there are more than one type of neutrinos. Three flavors of neutrinos have been proposed and observed to date. Each neutrino flavor is associated with a charged lepton, and named electron neutrino, muon neutrino, and tau neutrino, respectively. For instance, the neutrino produced in beta decay is always an electron neutrino.

The quarks and leptons are classified into three generations. The names and electric charges of the quarks and leptons are given in Table 2.1.

	Charge	First Generation	Second Generation	Third Generation
Quarks	+2/3	up (u)	charm (c)	top (t)
	-1/3	down (d)	strange (s)	bottom (b)
Leptons	-1	electron (e)	muon (μ)	tau τ
	0	electron neutrino (ν_e)	muon neutrino (ν_μ)	tau neutrino ν_τ

Table 2.1: The three generations of matter constituents: Quarks and Leptons.

2.1.2 Fundamental Interactions and Gauge Bosons

In addition to describing building blocks of matter, physics also attempts to understand the interactions between matter. The existence of two forces acting upon matter was obvious in classical physics, electromagnetism and gravity. However, it became apparent that additional forces existed, both to counter the electrostatic repulsion of protons inside the nuclei (the strong force) and to explain the radioactive beta decay (the weak force). Unlike the long-ranged electromagnetic and gravity, the strong force and the weak force are short ranged, typically at the scale of a proton (10^{-15} m) and an electron (10^{-18} m), respectively. In the SM, two major theories are combined, quantum chromodynamics (QCD) and the electroweak theory, to describe the strong force, weak force and electromagnetism.

QCD is a quantum field theory of the strong force. The spectrum of mesons and baryons is described as bound states of two or three quarks. A new quantum number called color was introduced to explain how quarks could coexist inside some hadrons in otherwise identical quantum states without violating the Pauli exclusion principle. Color appears in three states, commonly referred to as red, green and blue. Under this picture, the strong interaction between quarks is derived from local gauge invariance under SU(3) rotations in color space. The local invariance can be achieved by introducing 8 new gauge fields into the Lagrangian, corresponding to the eight types of gluons which mediate the strong force. The gluons themselves also carry color charge, giving rise to gluon self-interactions.

The electroweak theory is a unification of the processes behind electromagnetic and weak interactions. The familiar electromagnetic processes are mediated by the photon (γ) according to the theory of quantum electrodynamics (QED). The force carriers for the weak interaction are gauge bosons (W^+, W^-, and Z^0). The existence of W and Z gauge bosons was confirmed by experimental observations by the UA1 and the UA2 collaborations in proton-antiproton collisions at the Super Proton Synchrotron (SPS) at CERN in 1983 [16, 17].

Besides strong and electroweak interactions, gravitation is another fundamental interaction of the nature. Modern physics describes gravitation using the general theory of relativity (GR), whose approximation leads to the simpler and more familiar Newton's law of universal gravitation. Gravitation has not been incorporated into the framework of the SM because of the difficulty of integrating gravity and quantum mechanics using the usual framework of quantum field theory at high energies.

The characteristics of four fundamental interactions vary widely. Table 2.2 summarizes the conceptual schemes of the four interactions. The strong, electromagnetic and weak interactions are incorporated in the frame work of the SM.

Interaction	Theory	Mediators	Relative Strength	Range (m)
Strong	QCD	gluons	10^{38}	10^{-15}
Electromagnetic	QED	photons	10^{36}	∞
Weak	Electroweak theory	W and Z	10^{25}	10^{-18}
Gravitation	GR	gravitons[1]	1	∞

Table 2.2: The characteristics of the four fundamental interactions. The strong, electromagnetic and weak interactions are incorporated in the frame work of Standard Model of particle physics.

[1] hypothetical

2.1.3 Electroweak Symmetry Breaking

Unlike the massless gluon and photon, the W and Z bosons are heavy particles according to experimental observation. In any unbroken gauge field theory, the gauge bosons are required to be massless. Explicit mass terms for the bosons in the Lagrangian are not invariant under gauge transformation. The Higgs mechanism is introduced to solve this problem [18]. The electroweak symmetry group is spontaneously broken by the existence of a Higgs field with a non-zero vacuum expectation value. When expanding the Lagrangian around its vacuum state, effective mass terms for the electroweak gauge bosons $W^{\pm}$ and Z appear. Three of the initial four degrees of freedom of the Higgs fields are transformed into the longitudinal components of the weak gauge bosons $W^{\pm}$ and Z. The remaining degree of freedom gives rise to a new physical state, the Higgs boson, with charge and spin 0. The Higgs boson is the only SM particle that has not yet been observed. Experimetal observation of the Higgs boson and understanding electroweak symmetry breaking is one of the main goals of the LHC.

2.2 The Top Quark

2.2.1 Discovery of the top quark

Just as charm and bottom quarks were discovered as the bound states of quarks and anti-quarks pairs, physicists first searched for a $t\bar{t}$ meson in electron-positron collisions, but neither the experiments at Positron Electron Project (PEP) at SLAC nor Positron Electron Tandem Ring Accelerator (PETRA) at DESY found evidence for $t\bar{t}$ meson [19]. The e^+e^- collisions at 52 GeV center of mass energy at KEK set the lower limit on the top meson mass at 25.8 GeV [20]. Was it more massive? Hopes were placed in a new generation of accelerators: With the Super $p\bar{p}$ Synchrotron (S$p\bar{p}$S) at CERN, a

center of mass energy of 560 GeV was achieved[1], if the $t\bar{t}$ meson existed, it should have been produced and observed. Another possibility was given by the decay of the W and Z bosons, discovered with the SPS in 1983, for instance in $Z \to t\bar{t}$ or $W \to t\bar{b}$. Experiments studying these processes found no evidence for the top quark.

In 1985, Fermilab turned on its new superconducting $\sqrt{s} = 1.8$ TeV collider called the Tevatron Collider. The experiments CDF and D0 had as one of their goals the detection of the direct production of $t\bar{t}$ pairs decaying into observable final state particles, such as leptons and particle jets produced by quarks. The key features of the CDF and D0 detectors were their inner trackers, tailored to detect B mesons. Typically, a B meson has a half-life, $\tau \sim 10^{-12}$ s, that allows it to travel a distance of a few mm, that can be measured inside the detector with good precision. This information can be used to "tag" a particle jet as originating from a b-quark. The first observations of the top quark were reported by CDF [12] and D0 [13] in 1995. The large mass of the top quark, nearly 175 GeV, separates itself from all other quarks: it is the most massive fermion, nearly 40 times heavier than the closest competitor – the bottom quark. This peculiar characteristic of the top quark makes it behave quite differently than any other quark, as will be described Section 2.2.3.

2.2.2 Production of top quarks

At hadron colliders, top quarks are predominately produced via strong interactions. In these processes, top quarks are always produced in quark-antiquark pairs. The two main production channels for this process at leading-order are gluon-gluon fusion and quark-antiquark annihilation, as shown in Figure 2.1. At the Tevatron, top quark pairs are produced mainly through quark-antiquark annihilation. Theoretical calculations predict that the $t\bar{t}$ pairs will be produced via quark-antiquark annihilation 85% of the time at $\sqrt{s} = 1.96$ TeV [4]. The ratio of $t\bar{t}$ production via quark-antiquark annihilation and

[1] An upgrade raised this number to 900 GeV

gluon-gluon fusion has been measured experimentally and the results is consistent with the theoretical calculations [21]. At the LHC the most common production mechanism is gluon-gluon fusion, which accounts for about 90% of the total cross section [22].

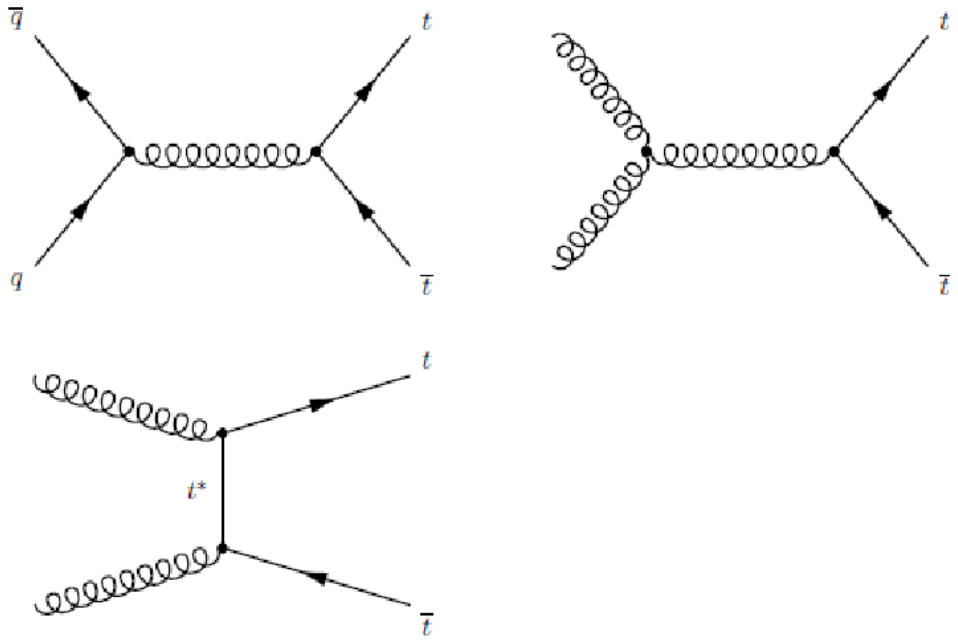

Figure 2.1: The $t\bar{t}$ pair production diagrams at leading order in pp collisions.

Next-to-leading-order (NLO) calculations have made predictions for this cross section at different energies and both pp and $p\bar{p}$ collisions. The precision of the NLO predictions has reached the level of 10%, which is dominated by the uncertainties on the probability distributions in momentum-space of the partons inside the protons (PDF). Figure 2.2 shows the theoretical prediction of the $t\bar{t}$ production cross section as a function of center of mass energy in both pp and $p\bar{p}$ collisions, compared to measurements at the Tevatron and the LHC [23]. For pp collision at $\sqrt{s} = 7$ TeV, the theoretical production cross section is about 160 pb.

The electroweak production of single top quarks is also predicted by the SM. The production cross section is predicted to be ~ 20 pb in $\sqrt{s} = 7$ TeV pp collisions, much smaller than that for pair production [24]. The experimental signature of single top

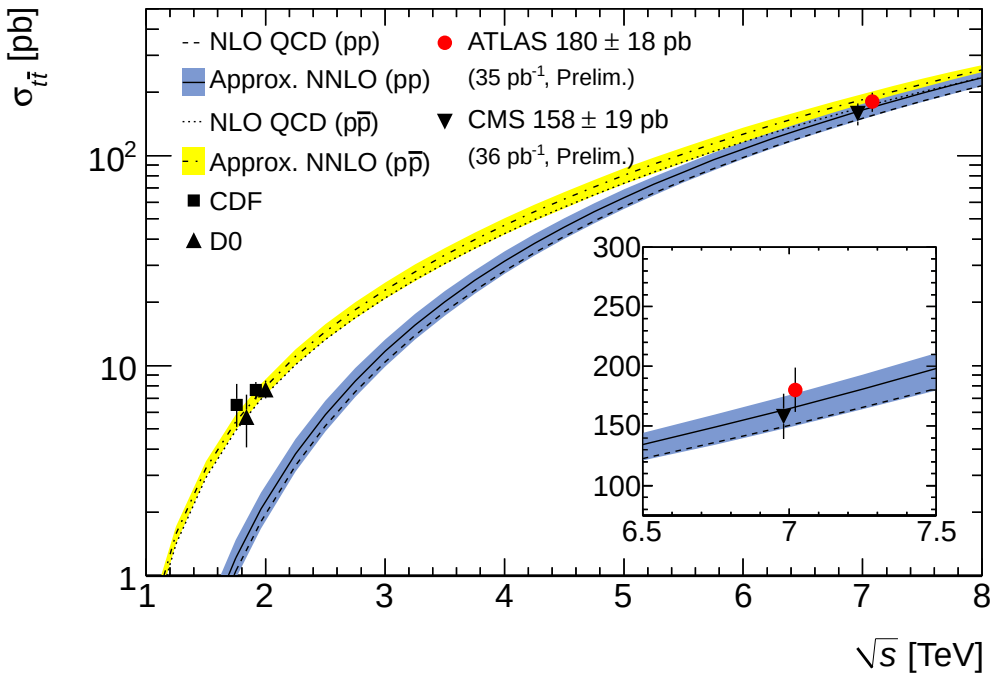

Figure 2.2: Theoretical predictions of $t\bar{t}$ production cross section assuming a top mass of 172.5 GeV as a function of $\sqrt{s}$. The predictions are compared to measurements from ATLAS and CMS in proton-proton collisions, and CDF and D0 in proton-antiproton collisions.

quark production suffers from much more challenging background contamination. The observation of single top quark production was only made recently in 2009 at D0 [25] and CDF [26].

2.2.3 Decay of Top Quark

The decay of the top quark is mediated by the electroweak interaction and the decay vertex includes a W boson. The strength of such a decay is proportional to the elements in the Cabibbo-Kobayashi-Maskawa (CKM) matrix:

$$\begin{pmatrix} |V_{ud}| & |V_{us}| & |V_{ub}| \\ |V_{cd}| & |V_{cs}| & |V_{cb}| \\ |V_{td}| & |V_{ts}| & |V_{tb}| \end{pmatrix} \sim \begin{pmatrix} 0.947 & 0.226 & 0.004 \\ 0.226 & 0.973 & 0.041 \\ 0.009 & 0.041 & 0.999 \end{pmatrix} \tag{2.1}$$

This matrix encodes the strength of the flavor-changing weak interaction between quarks of different flavors. In the case of the top quark decay, $|V_{tb}| \gg |V_{td}|$ and $|V_{ts}|$, so the decay $t \to Wb$ is completely dominant and its predicted branching ratio is BR($t \to Wb$)>99.8% [27]. Hence only $t \to Wb$ decays have been considered in the identification of top quarks, though searches for other decay modes have been undertaken.

The top quark decay width can be explicitly calculated, neglecting the b quark mass:

$$\Gamma_t = \frac{G_F m_t^3}{8\pi\sqrt{2}} \left(1 - \frac{m_W^2}{m_t^2}\right)^2 \left(1 + 2\frac{m_W^2}{m_t^2}\right) \left[1 - \frac{2\alpha_s}{3\pi}\left(\frac{2\pi^2}{3} - \frac{5}{2}\right)\right], \tag{2.2}$$

where G_F is the Fermi coupling constant, m_W is the mass of the W boson, m_t is the mass of the top quark, and α_s is the strong interaction coupling. For a top quark mass of 170 GeV, the decay width of this vertex yields $\Gamma = 1.7$ GeV, meaning that the top quark is unstable, with a corresponding lifetime of $\tau = \Gamma^{-1} = 4 \times 10^{-25}$ s. On the other hand, a hadron of typical radius ~ 1 fm cannot form in less than 10^{-22} s, which explains why a meson containing a top quark could not form and has never been observed. Thanks

to the high value of its mass, the top quark is the only quark that can be observed as a "bare" quark. Moreover, since the mass of the top quark is even larger than the sum of the masses of the W boson ($\sim$ 80.4 GeV) and b-quark ($\sim$ 4.5 GeV), the W boson from the top quark decay is "on shell"; this is an important characteristic of $t\bar{t}$ events that makes the precision measurement of the top quark mass possible. The W boson will in turn decay to two quarks 2/3 of the time and a charged lepton and its associated neutrino 1/3 of the time.

The experimental signature of $t\bar{t}$ events thus emerges. They are produced as top antitop pairs, each one decaying immediately to a real W boson and a b-quark. The b-quark hadronizes to a b-jet. The resulting W boson decays define the $t\bar{t}$ final state: There can be two hadronic decays (all hadronic channel), one leptonic and one hadronic decay (lepton+jets channel), and two leptonic decays (dilepton channel). The leptonic decays considered are usually based on only electrons or muons and their associated neutrinos, due to the experimental difficulty of identifying tau leptons. The branching ratios for these decay channels of the $t\bar{t}$ system are summarized in Figure 2.3.

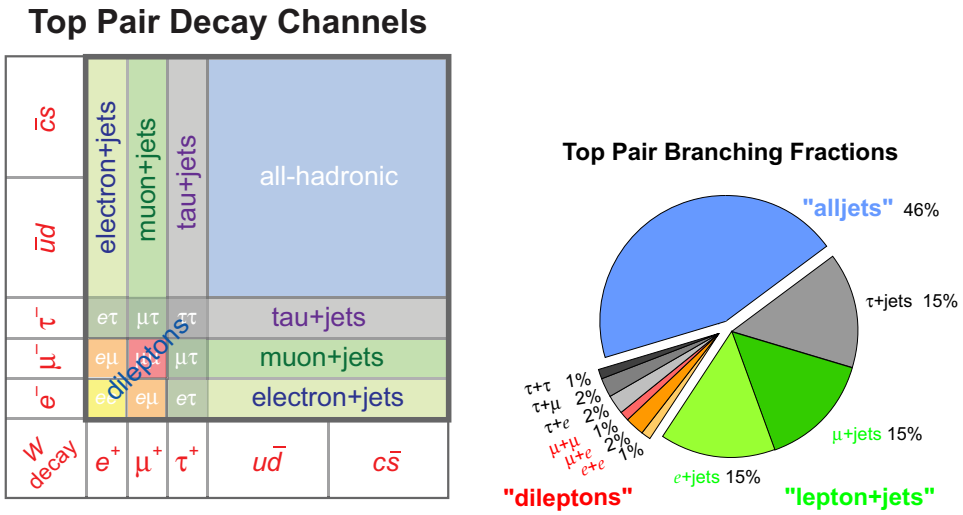

Figure 2.3: The $t\bar{t}$ pair decay channels (left) and branching ratios (right).

Due to the differences in the decay products, the experimental signature varies in

the three channels. The event topology and background processes that are associated with the three channels are summarized in Table 2.3. All of the three decay channels have been experimentally observed [28]. They have their own characteristics and are all interesting to study, allowing for cross-checks between channels. The focus of this thesis will be the dileptonic channel, which will be covered in more detail in Chapter 4.

Channel	Event topology	Dominate background
All hadronic	4 jets + 2 b-jets, no isolated leptons, no E_T^{miss}	QCD multijet
Lepton+jets	2 jets + 2 b-jets, 1 lepton, E_T^{miss}	W+jets
Dilepton	2 b-jets, 2 leptons, E_T^{miss}	Z+jets

Table 2.3: Summary of $t\bar{t}$ decay channels and their principal backgrounds.

2.3 Measurements of the Top Quark Production Cross Section

2.3.1 Theoretical Motivation

Since the observation of the top quark, intense efforts have been made to measure the top quark pair production cross section for a number of reasons.

First of all, a top quark cross section measurement is an excellent testing grounds for Standard Model physics. Top quark pair production is one of the most precisely predicted QCD processes, as comparing the measured cross section with the pertubative QCD calculation is a strong test of QCD theory. Since the top quark is by far the most massive known fermion, it provides a test for QCD at a higher energy scale than any other fermion.

Moreover, the top quark production cross section is sensitive to the Higgs sector and physics beyond the SM. Any deviations from the theoretically predicted value could be an indication of such new physics. For instance, the existence of a charged Higgs decay

channel $t \to H^+b$ would result in a measured cross section below the SM expectations while other models such as technicolor predict extra production mechanisms that will give a higher than expected cross section [29].

Finally, top quark cross section measurements give valuable inputs for other physics analyses. For instance, the characteristic signature of large missing transverse energy and high jet multiplicity of $t\bar{t}$ decay is an important background for a number of Supersymmetry (SUSY) searches [30]. Understanding top quark pair production is crucial for these searches.

2.3.2 Tevatron Measurements

The production cross section of top quark pairs has been measured at the Tevatron in $p\bar{p}$ collisions at $\sqrt{s} = 1.8$ TeV and $\sqrt{s} = 1.96$ TeV. Furthermore, $t\bar{t}$ production has been measured in all the three decay channels with various techniques. For instance, Figure 2.4 summarizes the $t\bar{t}$ cross section measured with different techniques and decay channels by the CDF experiment [28].

The experimental results have also been compared with theoretical predictions. Figure 2.5 shows the measured $t\bar{t}$ production cross section at the Tevatron collider and the theoretically predicted values [28]. The cross section measured with various techniques are consistent with each other and are in good agreement with the SM predictions.

2.3.3 Measurements at the LHC

The LHC is the only facility to produce $t\bar{t}$ pairs other than the Tevatron Collider. It was turned on in December 2009 with $\sqrt{s} = 900$ GeV and started pp collisions at $\sqrt{s} = 7$ TeV in March 2010. Due to the higher energies reached by the LHC, top quarks will be produced with much larger cross section (~ 160 pb), enabling precision studies of its properties in a high energy region than explored in the Tevatron experiments.

Both ATLAS and CMS experiments at the LHC have confirmed the observation of $t\bar{t}$

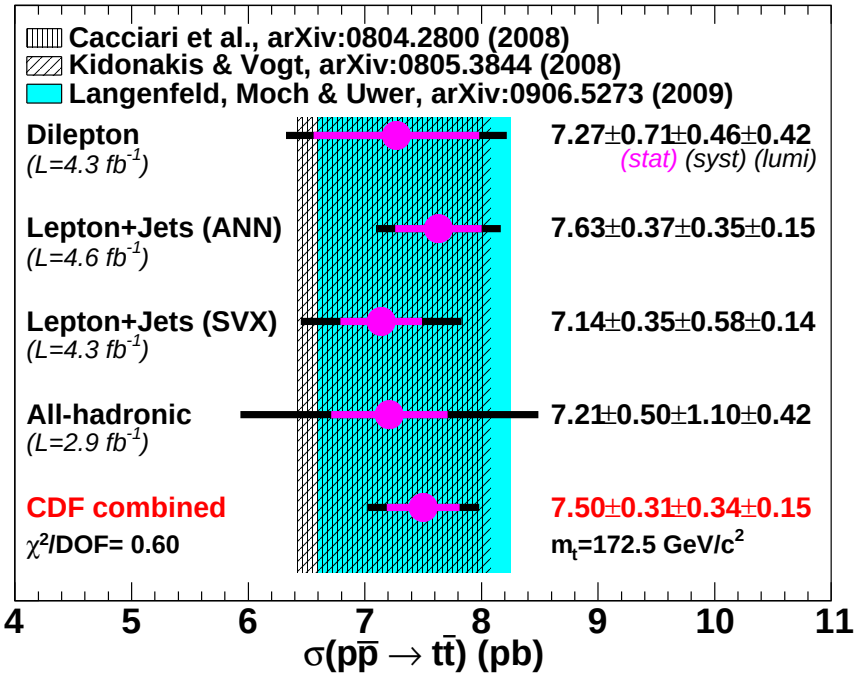

Figure 2.4: The $t\bar{t}$ cross section measured by the CDF experiment with various techniques.

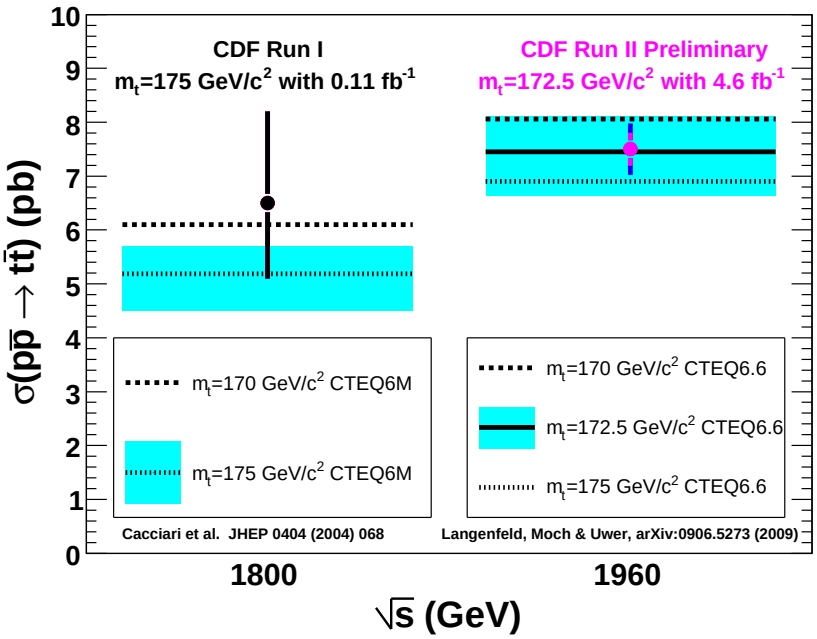

Figure 2.5: The approximate next-to-next-leading-order (NNLO) theoretical prediction and the measured cross-section at the Tevatron by CDF.

pairs in summer 2010 reports [31, 32]. By the end of 2010, the ATLAS experiment has collected about 35 pb^{-1} of data with 7 TeV pp collisions. This amount of data makes a first measurement of $t\bar{t}$ cross section possible with different techniques.

This dissertation will present one of the techniques to measure the $t\bar{t}$ cross section in the dilepton final states. In this measurement, we identify the candidate $t\bar{t}$ dilepton events, estimate the background contributions, selection acceptances and related systematic uncertainties and then simultaneously measure the $t\bar{t}$ cross section and the b-tagging efficiency using the observed b-tagged jets distribution.

Chapter 3

The ATLAS Experiment

3.1 The Large Hadron Collider

The Large Hadron Collider (LHC) is the largest particle accelerator in the world. It has been built in a circular tunnel about 100 meters under ground, across the border between France and Switzerland. The 27 kilometer circular tunnel was previously used by the Large Electron-Positron Collider (LEP).

The two colliding proton beams in the LHC is prepared by a chain of accelerators[1]. The first step in this process is stripping electrons off hydrogen atoms to create protons, and accelerate the protons to 50 MeV. The protons are then accelerated to 1.4 GeV by the Proton Synchrotron Booster (PSB). From the PSB, the beams is injected into the Proton Synchrotron (PS) where the protons reach an energy of 26 GeV. In the next step, the Super Proton Synchrotron (SPS) accelerates the protons to 450 GeV. Finally, the proton beam is injected into the LHC ring. The two counter circulating beams are then accelerated in separate beam pipes. The beams are kept in a circular orbit by a strong magnetic field created using superconducting magnets. The peak magnetic dipole field strength is about 8.3 Tesla. A schematic view of the accelerators is shown in Figure 3.1.

[1] Occasionally beams of lead ions are collided instead.

The protons in each beam are concentrated in bunches, with each bunch containing about 10^{11} particles. One important parameter to characterize the performance of the accelerator is the instantaneous luminosity, defined by the number of particles per unit area per unit time time.

$$\mathcal{L} = fn\frac{N_1 N_2}{A}, \tag{3.1}$$

where f is the revolution frequency, n is the number of bunches in one beam in the storage ring, N_i is the number of particles in each colliding bunch, and A is the cross section of the beam. The design luminosity of the LHC is 10^{34} cm^{-2}s^{-2}. The design center of mass energy is 14 TeV. However, during the initial running period, both the center of mass energy and the luminosity was lower. The center of mass energy for the data collected in 2010 was 7 TeV, and the peak luminosity reached 10^{32} cm^{-2}s^{-2}. At this luminosity, a large fraction of the bunch crossings contains more than one *pp* interactions. The general term pile-up refers to the additional interactions "piled up" in each bunch crossing.

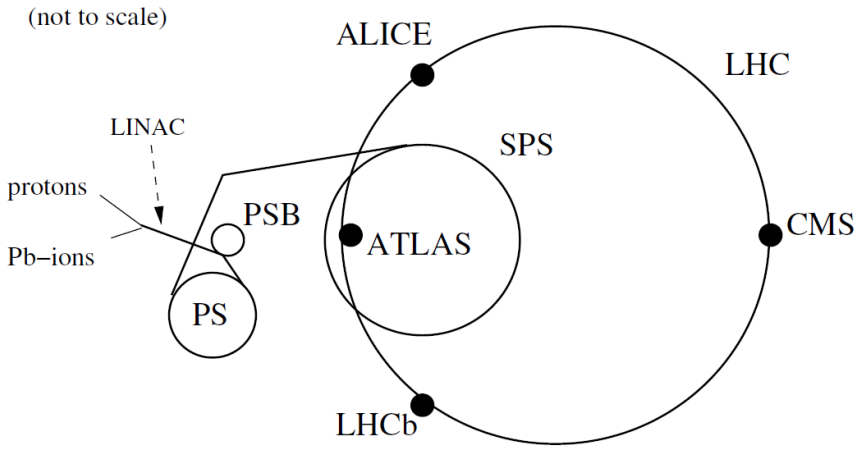

Figure 3.1: Schematic view of the particle accelerators forming the LHC complex.

Four large experiments (ATLAS, CMS, LHCb and ALICE) have been constructed to study the collisions at the LHC. The counter-circulating beams collide at four interaction points in the LHC ring, as shown in Figure 3.1. The LHCb (Large Hadron Collider

beauty) is an experiment specialized in studying the physics of the bottom quark. ALICE (A Large Ion Collider Experiment) is a detector that is optimized to study heavy ion collisions. ATLAS (A Toroidal LHC ApparatuS) and CMS (Compact Muon Solenoid) are large general-purpose detectors, designed to cover a wide range of physics programs at the LHC. The ATLAS experiment is described in detail in Section 3.2.

3.2 The ATLAS Detector

The ATLAS [33] is a multipurpose detector designed to explore a wide range of physics including tests of the Standard Model and searches for physics beyond the Standard Model. The overall layout of the ATLAS detector is shown in Figure 3.2. It is built up of several subdetectors, configured in concentric layers around the interaction point, each optimized for the detection of a specific type of particle. From the interaction point outwards, the first subdetector is the inner detector, followed by the calorimeter systems, divided into electromagnetic and hadronic components. The outer tracking detector is the muon spectrometer, designed to identify and measure tracks of muons. Both the inner detector and the moun spectrometer operate in magnetic fields, provided by a solenoidal and a toroidal magnet system, respectively.

The physics goals for the ATLAS experiment include:

- Understanding the mechanism behind electroweak symmetry breaking. This leads to a major focus on searches for the Higgs boson.
- Searches for other phenomena related to symmetry breaking, such as supersymmetry and supersymmetric particles.
- Searches for new heavy gauge bosons.
- Searches for evidence for composite quarks and leptons.
- Investigating CP violation in B decays.

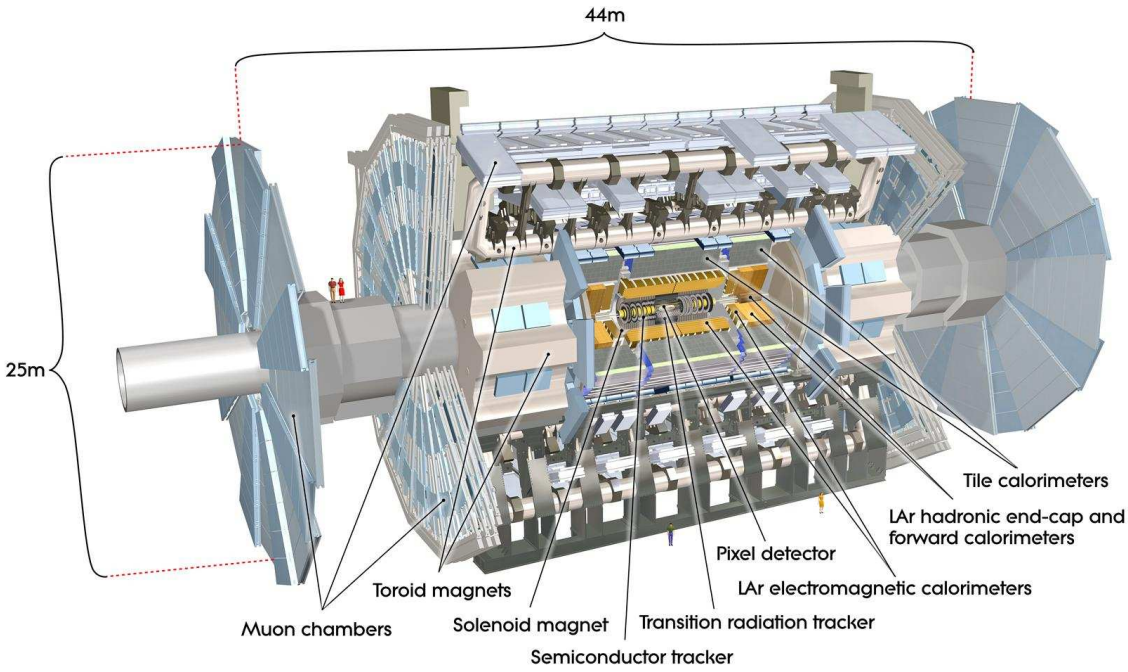

Figure 3.2: The ATLAS detector. The diameter and barrel toroid lengths are both 25 m and the overall length is 44 m. The overall weight of the ATLAS detector is approximately 7000 tons.

- Precision measurements and tests of the Standard Model, including QCD, electroweak, flavour and top quark physics.

The performance requirements for the ATLAS detector are motivated by these physics goals, which requires the identification and measurement of a wide range of particles that are expected to be created in the *pp* collisions at the unprecedented energies and luminosity. This imposes strict requirements on the detector's precision, speed, performance, radiation hardness, efficiency and acceptance. An additional challenge is the real-time selection of collisions, which requires a reliable trigger system. The subdetector and trigger systems are discussed in more detail in Section 3.2.2 through 3.2.6.

3.2.1 ATLAS Coordinate System

Throughout this thesis, the standard ATLAS coordinate system is employed:

- The z-axis is defined by the beam direction and the x and y coordinates lie in the plane transverse to the beam direction.
- The x-axis points from the interaction point to the center of the LHC ring.
- The y-axis points upwards from the beam.

From the rectangular coordinates, spherical (r, ϕ, θ) is defined as usual. The pseudorapidity η is defined in terms of the polar angle θ:

$$\eta = -\ln(tan(\frac{\theta}{2})) \tag{3.2}$$

The distance ΔR will be sued frequently and is defined as:

$$\Delta R = \sqrt{(\Delta\eta)^2 + (\Delta\phi)^2} \tag{3.3}$$

The transverse energy (E_T) and transverse momentum (p_T) are defined as the projection of energy and momentum in the transverse plane, respectively.

3.2.2 The Inner Detector

The Inner Detector (ID) instruments the innermost part of ATLAS. It measures the charge, the momentum and the direction of each charged particle trajectory. The ID is also responsible for reconstructing both primary and secondary vertices. The ID has an inner radius of 45 mm, as close as 10 mm to the beam pipe and extends to a radius of 1150 mm, and is contained inside a solenoidal magnetic field of 2 T. It consists of 3 independent but complementary components: the pixel detector, the semiconductor tracker (SCT) and the transition radiation tracker (TRT). Their configuration is illustrated in Figure 3.3.

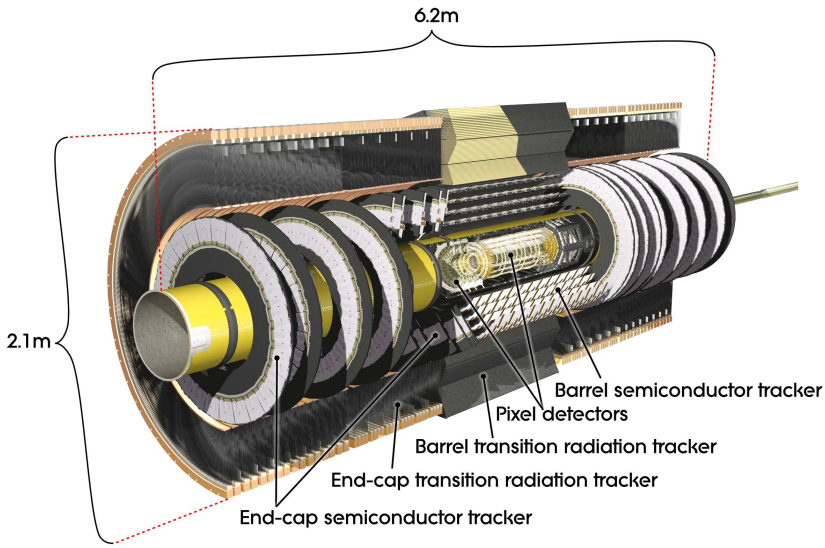

Figure 3.3: Cut-away view of the ATLAS Inner Detector.

The momentum and vertex resolution requirements call for high-precision measurements to be made with fine-granularity detectors, given the very large track density expected at the LHC. The pixel detector consists of three concentric layers around the beam axis and three discs perpendicular to the beam axis on each side of the interaction point. The 1744 modules that constitute the pixel detector each consist of a 250 μm layer of silicon implanted with readout pixels that measure 50×400 μm^2, adding up to a total of 80 million pixels. Electron-hole pairs are created in the silicon when charged particles

pass through it and a current is induced due to the p-n junction in the doped silicon, which is then read out by the high speed electronics. The pixel detector's primarily role is for precise identification of the primary vertex and secondary vertices.

The middle component of the inner detector is the SCT, which is composed of four concentric barrels around the beam axis and nine endcap disks along the beam line on each side. Its detection principle is similar to that of the pixel detector, although the lower particle density allows for long, narrow silicon strips rather than small rectangular pixels. The strips are configured in two layers under a small angle with respect to each other, such that a position measurement along the strip length can be obtained from hits in overlapping strips.

The technology employed in the outer component of the inner detector, the TRT, is twofold: gaseous straw tubes layers are interleaved with material that induces transition radiation[2]. The TRT is operated with a gas mixture of 70% Xe, 20% CO_2 and 10% CF_4 with a total volume of 3 m^3. The barrel contains 73 such layers and the 20 wheels on each endcap are covered with 160 such planes, adding up to approximately 350k readout channels. When charged particles pass through, the gas inside the tubes is ionized and a voltage difference between the tube and the anode wire in its center causes the free electrons to drift towards the wire and create an electric signal. The intensity of the transition radiation photons is proportional to the Lorentz factor of the traversing particle, which is much higher for electrons than for pions, at equivalent energies, due to their mass difference. This discrimination power between electrons and hadrons from the TRT can be combined with information from other subdetector systems for electron identification.

By combining the pixel detector and the SCT at small radii with the TRT at a larger radius, high-precision, robust pattern recognition can be achieved.

[2]Transition radiation is produced by relativistic charged particles when they cross the interface of two media of different dielectric constants.

3.2.3 The Calorimetery System

A view of the sampling calorimeters is presented in Figure 3.4. These calorimeters cover the range $|\eta| < 4.9$, using different techniques suited to the widely varying requirements of the physics processes of interest and of the radiation environment over this large η-range. The Atlas Calorimetery system consists of a LAr electromagnetic calorimeter, Tile Calorimeter, LAr Hadronic endcap calorimeter and LAr forward calorimeter.

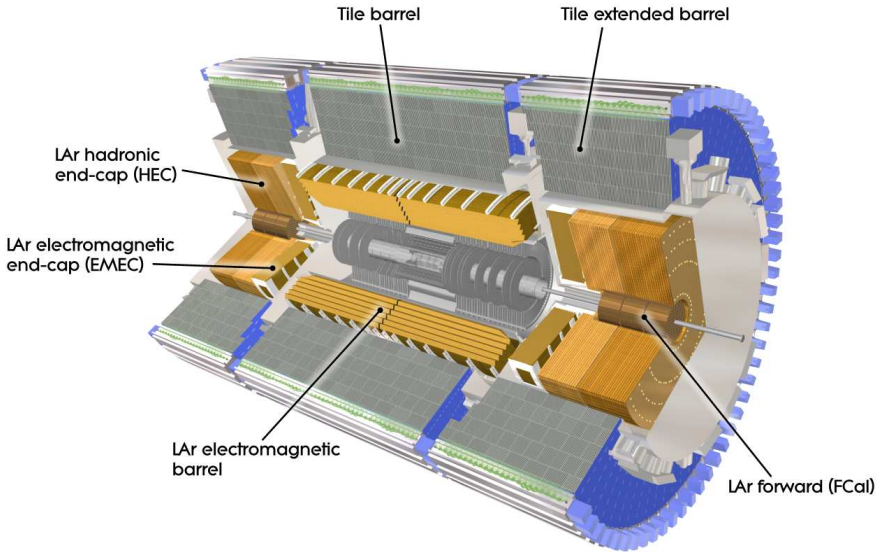

Figure 3.4: Cut-away view of the ATLAS calorimeter system.

LAr electromagnetic calorimeter

The EM calorimeter is divided into a barrel part ($|\eta| < 1.475$) and two endcap components ($1.375 < |\eta| < 3.2$), each housed in their own cryostat. The barrel calorimeter consists of two identical half-barrels, separated by a small gap (4 mm) at z = 0. Each endcap calorimeter is mechanically divided into two coaxial wheels: an outer wheel covering the region $1.375 < |\eta| < 2.5$, and an inner wheel covering the region $2.5 < |\eta| < 3.2$. The EM calorimeter is a lead-LAr detector with accordion-shaped kapton electrodes and lead absorber plates over its full coverage. The segmentation and geometry of the barrel

module is shown in Figure 3.5. The accordion geometry provides complete ϕ symmetry without azimuthal cracks.

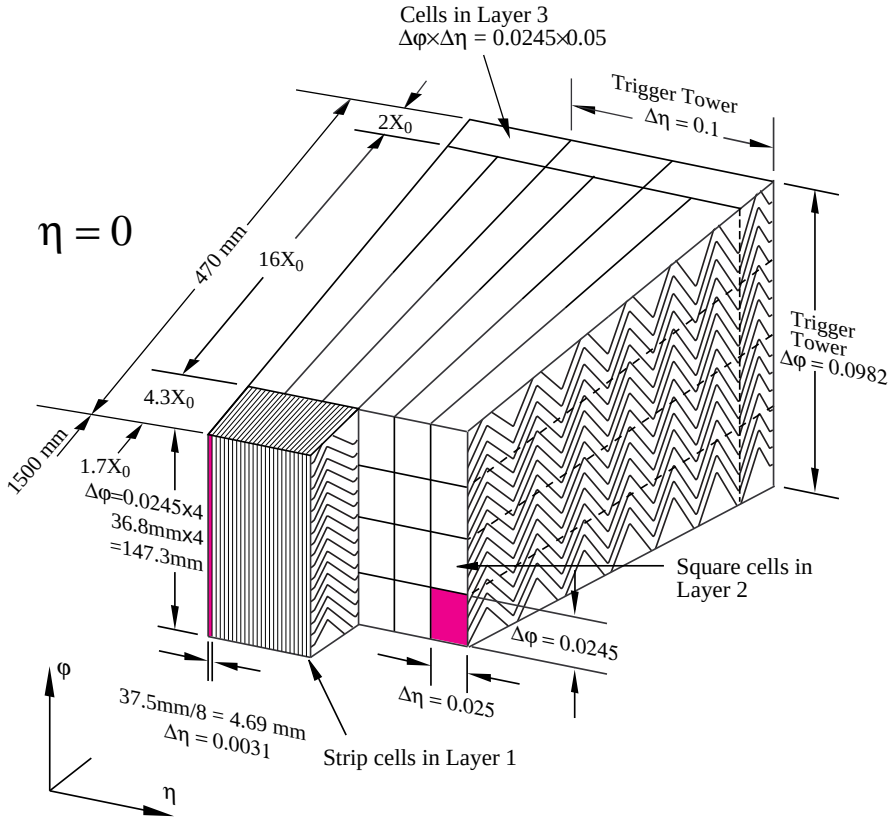

Figure 3.5: Sketch of a barrel module where the different layers are clearly visible with the ganging of electrodes in phi. The granularity in η and ϕ of the cells of each of the three layers and of the trigger towers is also shown.

Hadronic calorimeters

Tile calorimeter. The tile calorimeter is placed directly outside the central EM calorimeter envelope. Its barrel covers the region $|\eta| < 1.0$, and its two extended barrels the range $0.8 < |\eta| < 1.7$. It is a sampling calorimeter using steel as the absorber and scintillating tiles as the active material. The barrel and extended barrels are divided azimuthally into 64 modules. Two sides of the scintillating tiles are read out by wavelength shifting fibres into two separate photomultiplier tubes. In η, the readout cells built by grouping fibres into the photomultipliers are pseudo-projective towards the interaction region.

LAr hadronic endcap calorimeter. The Hadronic endcap Calorimeter (HEC) consists of two independent wheels per endcap, located directly behind the endcap electromagnetic calorimeter and sharing the same LAr cryostats. Each wheel is divided into two segments in depth. In each wheel, the copper plates are interleaved with LAr gaps, providing the active medium for this sampling calorimeter.

LAr forward calorimeter. The Forward Calorimeter (FCal) is integrated into the endcap cryostats. It consists of three modules in each endcap: the first, made of copper, is optimized for electromagnetic measurements, while the other two, made of tungsten, measure predominantly the energy of hadronic interactions. Each module consists of a metal matrix, with regularly spaced longitudinal channels filled with the electrode structure consisting of concentric rods and tubes parallel to the beam axis. The LAr in the gap between the rod and the tube is the sensitive medium. This geometry allows for excellent control of the gaps, which are as small as 0.25 mm in the first section, in order to avoid problems due to ion buildup.

Signal Tower and Topological Cluster

The calorimetry system is responsible for the reconstruction of jets, and contains about 200,000 cells in various sizes and geometries. In order to provide practical inputs for the jet finding algorithm, all these cells are combined into larger signal inputs. Two types of inputs are usually used: signal towers and topological clusters.

For the signal towers, the calorimeter cells are collected into bins of a regular 2D $\delta\eta \times \delta\phi = 0.1 \times 0.1$ grid, forming 6400 towers in total. The topological cluster is an algorithm that groups cells in clusters based on their neighbor relations and on the significance of their energy contents. In this way, the topological clustering enables noise suppression in contrast to the signal towers. The clustering procedure is as follows:

1. At first, each cell energy E_{cell} is compared to its stored characteristic value $\sigma_{\text{noise,cell}}$ due to the electronic noise and pile-up. The clustering starts by a seed cell with

the signal-to-noise ratio $E_{\text{cell}}/\sigma_{\text{noise,cell}}$ above four.

2. The nearby cells around the seed cells are then included if $\sigma_{\text{noise,cell}} > 2$.

3. Finally, all cells with $\sigma_{\text{noise,cell}} > 0$ surrounding the cluster are grouped as the cluster boundary.

The above clustering sequence is often referred to as 4/2/0 clusters, and is the default one being used in ATLAS, although other clustering procedures and thresholds exist.

3.2.4 The Muon Spectrometers

The muon spectrometer forms the outer part of the ATLAS detector, as shown in Figure 3.6. It is designed to detect muons exiting the calorimeters and to measure their momentum in the pseudorapidity range $|\eta| < 2.7$, and trigger on these muons in the region $|\eta| < 2.4$. The performance goal is a stand-alone transverse momentum resolution of approximately 10% for 1 TeV tracks. High measurement accuracy, simplicity of construction and cost effectiveness were taken into consideration when designing the muon detection chambers.

Four types of detection chambers are used in the Muon Spectrometer: Monitored Drift Tube Chambers (MDT) and Cathode Strip Chambers (CSC) for momentum measurements and Resistive Plate Chambers (RPC) and Thin Gap Chambers (TGC) for triggering. The chambers in the barrel are arranged in three concentric cylindrical shells around the beam axis at radii of approximately 5 m, 7.5 m, and 10 m. In the two endcap regions, muon chambers form large wheels, perpendicular to the z-axis and located at distances of 7.4 m, 14 m, and 21.5 m from the interaction point.

3.2.5 Magnet System

Both the Inner Detector and Muon Spectrometers use bending tracks of charged particles in the magnetic field to measure their momentum. The magnetic field is provided by

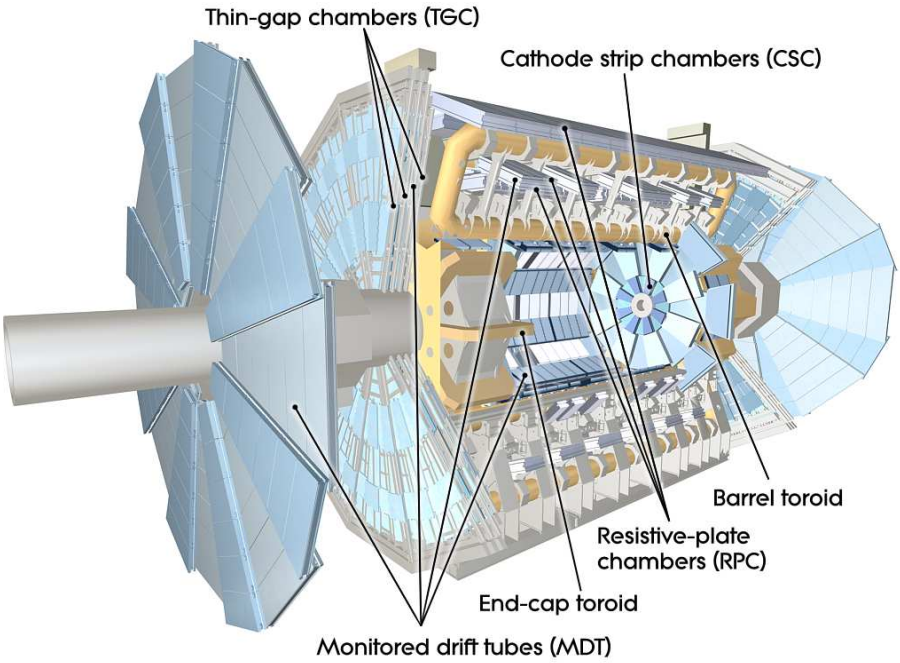

Figure 3.6: Cut-away view of the ATLAS muon spectrometers.

an inner superconducting central solenoid and a superconducting air-core toroid. The solenoid surronds the inner detector and provides a magnetic field with a peak field strength of 2.6 T. The toroid magnet system includes one barrel and two endcaps, each contain eight coils symmetrically arranged outside the calorimeters at a radius of 20 m. The peak magnetic fields are 3.9 T and 4.1 T for the barrel and the endcap toroids, respectively.

As a result of the layout of the magnetic fields, charged particle tracks are bent in the detector. The tracks are bent in the r-ϕ plane as the particles transverse the ID and in the r-z plane as they traverse the fields.

3.2.6 The Trigger and Data Acquisition System

The trigger system is essential for reducing the enormous data flow and to select potentially interesting events from the large rate of inelastic collisions. The initial bunch crossing rate in the LHC is 40 MHz but it must be reduced to about 100 Hz for perma-

nent storage of collision records. This puts challenging requirements on the triggers to both reject low energy collision events with a high rejection factor and simultaneously maintain maximum efficiency for selecting the rare physics processes one wishes to study.

The trigger system in ATLAS is based on three separate levels of online selection: The first level trigger (LVL1), the second level trigger (LVL2) and the Event Filter (EF). Each trigger level refines the previous decision by applying further selection criteria. A schematic figure of the trigger system is shown in Figure 3.7.

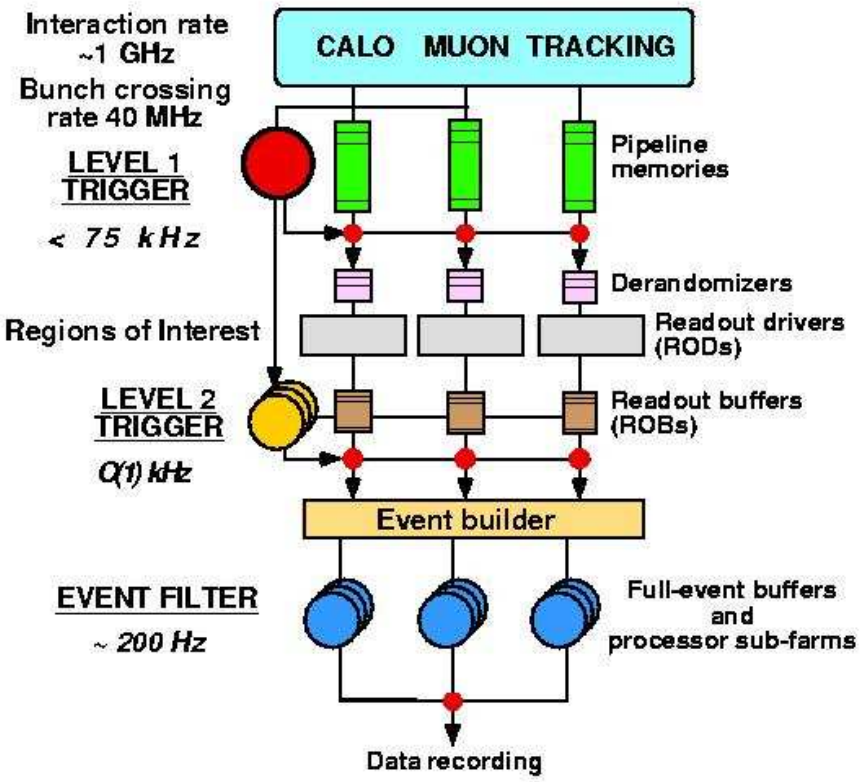

Figure 3.7: The schematic diagram of the ATLAS trigger system.

The LVL1 trigger decision is based on reduced granularity information from different ATLAS subdetectors. The muon trigger chambers are used to identify high-p_T muons. Basic information from the electromagnetic and hadronic calorimeters are used to identify high-p_T electrons, photons, jets and tau leptons decaying into hadrons. At the LVL1

trigger level, most physics requirements can be met using relatively simple selection criteria. Events that are selected by the LVL1 trigger are read out from the front-end electronics into readout drivers (RODs) and then into readout buffers (ROBs). The events are kept in the ROBs until a decision is made by the LVL2 trigger whether to keep or reject the events selected by the LVL1 trigger.

As opposed to the hardware-implemented LVL1 trigger, the LVL2 trigger and the EF are implemented in software. The data used by the LVL2 trigger is provided by the LVL1 trigger as Region-of-Interest (RoI) information. The last step in the online selection process is made by the EF. The events selected by the EF in this final stage are written to storage and accessible for subsequent offline analysis. The total event rate will now have been reduced by the three trigger levels from an original rate of 40 MHz to 100 Hz. This corresponds to a data rate of 100 MB/s. Due to the lower instantaneous luminosity in the initial running period (see Section 3.1), only the LVL1 and LVL2 trigger were required to maintain a manageable event rate at the beginning of 2010. The EF level trigger was included when the instantaneous luminosity significantly increased in summer 2010.

3.2.7 ATLAS Computing

ATLAS uses an advanced computing system to handle and distribute the large amount of data produced in the LHC collisions. The yearly data volume is several PB (10^{15} bytes). The computing system is based on GRID technology, a way of sharing computing power and data storage capacity over the Internet [34].

ATLAS software uses an object-oriented approach and is mainly based on the `C++` language. Software development is built on a common framework, Athena. All processing of ATLAS data takes place within the Athena framework, from the software based high level trigger to the simulation of the detector response to various physics processes, and data analysis.

The data flowing from the trigger system is byte stream data. After the EF, the last stage of the trigger system, events are stored as Raw Data Objects (RDOs). After the event data has been passed through reconstruction algorithms, the results are stored as Event Summary Data (ESD). From the ESD, a reduced event representation is produced, known as Analysis Object Data (AOD), corresponding to about 100 kB/event. For the analyses performed by various physics groups, the AOD is further stripped into Derived Physics Data (DPD) and Tag Data (TAG).

Chapter 4

Data Samples and Event Selection

4.1 Collision Data

This analysis uses pp collision data with a center of mass energy of $\sqrt{s} = 7$ TeV taken between March 30th and October 31st, 2010. Peak instantaneous luminosity of $2 \times 10^{32}\text{cm}^{-2}\text{s}^{-1}$ was reached during this period of data taking. The ATLAS data taking runs are divided into luminosity blocks. Each luminosity block corresponds to about 2 minutes of data taking. The luminosity blocks are kept in the analysis if they were collected during periods in which the LHC was circulating stable colliding beams and ATLAS systems were producing data of sufficient quality.

The integrated luminosity was determined by measuring the observed interaction per beam-crossing independently with a variety of detectors using several different algorithms [35]. The total delivered integrated luminosity was about 47 pb^{-1} with 43 pb^{-1} recorded by ATLAS. Taking into account the luminosity block selection, the total integrated luminosity for the 2010 data sample is calculated to be $\mathcal{L}$=35.3 pb^{-1}. This integrated luminosity estimate has an uncertainty of 3.4% [36]. The data taking was separated into data periods in which trigger conditions remained stable. The periods were labeled as A-I and the periods A-E3 were dropped from the analysis to simplify the

trigger selection. The dropped periods corresponds to about 0.8 pb^{-1}.

4.2 Monte-Carlo Samples

Monte Carlo simulation samples have been used to develop and validate the analysis procedures, and to evaluate the contribution from some background processes. After event generation, all samples have been processed with the GEANT4 [37] simulation of the ATLAS detector, and then reconstructed and passed through the same analysis chain as the data [38].

For the generation of $t\bar{t}$ signal and single top events, MC@NLO [39, 24] v3.41 was used, with PDF set CTEQ66 [40], assuming a top quark mass of 172.5 GeV and normalizing the $t\bar{t}$ cross section to the prediction using the Hathor [41] code of 164.6 pb at approximate next-to-next-to-leading order (NNLO) in QCD. For single top the s, t and Wt channels are included, normalizing to the MC@NLO cross-section and using the "diagram removal scheme" [42] for Wt to remove overlaps with the $t\bar{t}$ final state.

For the generation of W+jets events, Drell-Yan events (Z/γ^*+jets), and QCD multijet events Alpgen v2.13 was used, invoking the MLM matching scheme [43] with matching parameters `RCLUS`=0.7 and `ETCLUS`=20, and using the parton density function set CTEQ6L1 [44]. For the vector boson + jet (QCD multijet) samples, the exclusive mode of generation was used for $2 \to 2$, $2 \to 3$,..., $2 \to 6$ (..., $2 \to 5$) processes, with $2 \to 7$ ($2 \to 6$) processes generated in inclusive mode. Detailed descriptions on the Monte Carlo samples used in this analysis are listed in Appendix B.

4.3 Trigger Requirements

During the 2010 period of ATLAS running, most of the data was collected with peak luminosities of around 10^{32} $\text{cm}^{-2}\text{s}^{-1}$. Single-lepton triggers with relatively low threshold and loose selection requirements were implemented without any pre-scaling. The selec-

tion of $t\bar{t}$ dilepton (ee, $e\mu$, and $\mu\mu$) candidate events requires a positive decision of a high level single high-p_T lepton trigger. Due to the rapidly increasing LHC luminosity and the commissioning of the trigger system, the detailed trigger requirements vary through the data-taking period. Table 4.1 summarizes the trigger requirements during the different data periods for the electron and muon trigger. For electrons, a level-1 electromagnetic trigger object of at least 13 GeV is always required, augmented by a more refined electromagnetic cluster selection and subsequently an event filter calorimeter-track match in later data. Muons are selected requiring a 13 GeV threshold muon trigger chamber track at LVL1, matched by a muon reconstructed in the muon spectrometer at the event filter level. For MC, the event filter level triggers are used, electrons are required to pass the "medium" quality cuts and have at least 15 GeV of transverse energy (EF_e15_medium) and muons are required to pass the "tight" quality selection and have at least 13 GeV of transverse momentum (EF_mu13_tight).

Data period	Muon Trigger	$\mathcal{L}$ [pb^{-1}]	Electron Trigger	$\mathcal{L}$ [pb^{-1}]
E4-E7	EF_mu10_MSonly	0.5	EF_e15_medium	0.5
F	EF_mu10_MSonly	1.5	EF_e15_medium	1.5
G1-G5	EF_mu13	4.3	EF_e15_medium	4.3
G6	EF_mu13_tight	1.2	EF_e15_medium	1.2
H	EF_mu13_tight	6.9	EF_e15_medium	6.9
I	EF_mu13_tight	20.7	EF_e15_medium	20.7

Table 4.1: Trigger used for the different data periods and their integrated luminosities, for MC EF_mu13_tight and EF_e15_medium were used.

4.4 Electron Selection

Starting from the sample triggered as described above, the reconstructed offline candidate electrons were selected with a set of quality requirements to ensure that candidates are consistent with the energy deposition of an electron in the calorimeters and there is a well-measured track associated with the electromagnetic cluster. The electron ID requirements have been tightened with an additional E/p cut and the requirement of at

least one hit in the innermost layer of the pixel detector (b-layer), in order to reduce fake electron background from multijet events, with an additional efficiency loss of ∼10%. This quality requirement is known as `RobustMedium` [45].

Electrons from prompt W boson decay are isolated from jet activity, unless there is an accidental overlap with one of the jets in the event. The three main sources of background for high momentum isolated electrons are hadrons faking an electron signature, electrons from heavy-flavor decays and photon conversions. In order to suppress the background from these sources we require that there is little energy flow in the vicinity of the electron candidate. As a gauge for the jet activity, we use the energy in a cone of $\Delta R \equiv \sqrt{\Delta\eta^2 + \Delta\phi^2} = 0.2$, `EtCone20`, centered around the electron, from which a subtraction is made of the energy associated with the electron itself. For the analysis described in this thesis, we use `EtCone20` < 4 GeV.

The electron candidates passing the quality and isolation requirements are further required to have $E_T > 20$ GeV, where the E_T is constructed as $E_T = E_{clus}/\cosh(\eta_{track})$, i.e. from the calorimeter cluster energy, E_{clus} and the direction of the electron track, η_{track}. In addition, the electron candidates are required to have $|\eta_{\text{cluster}}| < 2.47$, excluding the calorimeter crack region at $1.37 < |\eta_{\text{cluster}}| < 1.52$. Table 4.2 summarizes the selection requirements for the electron candidate in this thesis.

Electron Cuts	
Variable	Cut
Quality (isEM)	RobustMedium
Fiducial cuts	$1.52 < \|\eta\| < 2.47$ or $0 < \|\eta\| < 1.37$
Isolation	`EtCone20` < 4 GeV
E_T	> 20 GeV

Table 4.2: Electron identification cuts used in this analysis. The isolation requirement uses `EtCone20` as described in the text.

4.5 Jet Selection

Jets are reconstructed with the anti-k_t algorithm [46] with the distance parameter R=0.4, starting from topological energy clusters in the calorimeter reconstructed at the electromagnetic (EM) scale appropriate for the energy deposited by electrons or photons. The anti-k_T algorithm showed better or equivalent performance compared to other algorithms in terms of a large number of observable jet parameters, including reconstruction efficiency, sensitivity to flavour/fragmentation model, stability in jet area, robustness with respect to underlying event and pile-up contributions, and good adaptability to inclusion in trigger decisions [47, 48].

The jets reconstructed by the calorimeter are classified based on the quality of the reconstruction, and divided into three categories, known as "Ugly", "Bad" and "Good". "Ugly" jets correspond to real energy deposition in region where the energy measurement is not optimal, but these jets can be considered for the analysis. "Bad" jets refer to jets not associated to in-time energy deposits in the calorimeters caused by various sources ranging from hardware problems in the calorimeter, the LHC beam conditions, and the cosmic ray backgrounds. For jets with an transverse momentum of more than 20 GeV, the rate of mis-reconstructed jets is about 5% [49]. "Bad" jets was not considered in the analysis, they were used to reject the non-collision background which will be discussed in Section 4.8.

Electrons deposit energy in the Electromagnetic Calorimeters and thus could be reconstructed as jets. After the electron selection discussed in Section 4.4, we remove jets with an axis within $\Delta R < 0.2$ of the electron candidate to prevent double counting the energy deposition by the electron.

Jets are calibrated with Monte Carlo based p_T and η dependent correction factors to restore the full hadronic energy scale after passing through non-compensating calorimeters.

Most of the jets from dileptonic $t\bar{t}$ decay are generally more central and high-p_T. In

this analysis, in addition to the jet quality requirements, jet candidates are required to have $|\eta| < 2.5$ and $p_T > 20$ GeV. Most of the jets from dileptonic $t\bar{t}$ events are arising from b-quarks, making this channel ideal for the application of b-tagging given the expected improvement in the signal to background ratio. However, at the pre-selection stage of the analysis, no b-tagging requirement on the jets is applied. All the pre-selected events will be used to simultaneously measure the b-tagging efficiency and $t\bar{t}$ cross section.

4.6 Muon Selection

Muons are reconstructed from the tracks in the Muon Spectrometers and Inner Detector. Muon candidates are reconstructed by the MuID algorithm [5] which starts with a search for track segments in different layers of the muon chambers. These segments are then combined starting from the outermost layer, fitted to account for material effects, and matched with tracks found in the inner detector to form a combined muon candidate. The final candidates are refitted using the complete track information from both detector systems, and required to satisfy $p_T > 20$ GeV, $|\eta| < 2.5$ and the 'tight' quality cut criteria [45].

To reduce muon candidate background from the decays of hadrons produced in jets and to suppress the selection of muons from heavy flavor decays inside jets, the muons are required to be isolated. The corresponding calorimeter isolation energy in a cone of $R = 0.3$ is required to be less than 4 GeV, and the analogous sum of track transverse momenta in a cone of $R = 0.3$ is also required to be less than 4 GeV. In addition, it has been shown that requiring the muon candidates to have a distance ΔR greater than 0.4 from any jet with $p_{\mathrm{T}} > 20$ GeV further reduces the rate of muons from heavy flavor decays. This is illustrated in Figure 4.1.

Each pair of muons passing the above cuts are checked against a simple cosmic-muon rejection criteria. The event is removed if it contains a pair of muons having opposite

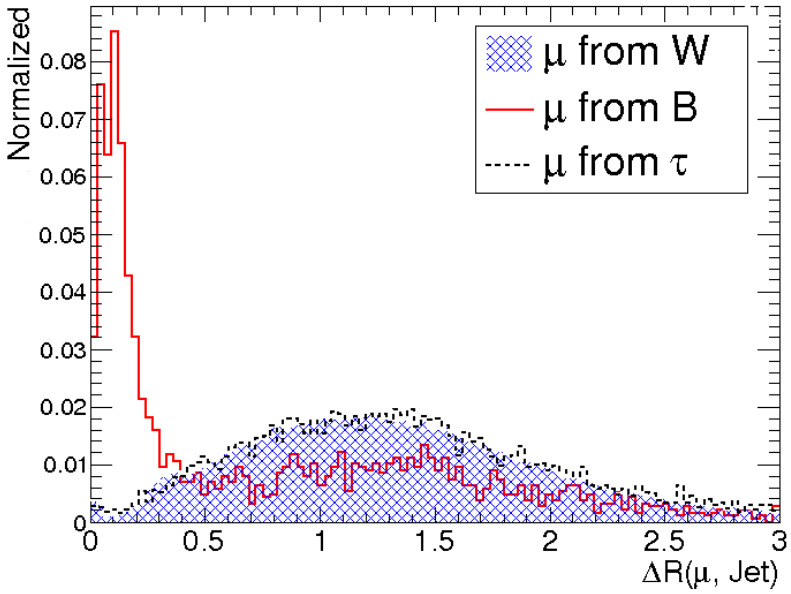

Figure 4.1: The ΔR distribution between the muon and the jet closest to it based on $t\bar{t}$ MC calculations. Muons from W boson, τ lepton, and heavy flavor decay are compared. The distributions are normalized to unity. The origins of the muons are identified by matching the reconstructed muons to the MC truth muons and then determining the parents of the truth particles.

signed impact parameters d_0, both fulfilling $|d_0| > 0.5$ mm and $\Delta\varphi > 3.10$ between their azimuthal directions.

The selection criteria for muon candidates in this analysis is summarized in Table 4.3.

Muon Cuts	
Variable	Cut
Quality	Tight
Fiducial cuts	$\|\eta\| < 2.5$
Isolation	$ptcone30 < 4$ GeV, $etcone30 < 4$ GeV, and $\Delta R_{\mu,jet} > 0.4$
p_T	> 20 GeV
Cosmic Rejection	$\|d_0\| > 0.5$mm and $\Delta\varphi > 3.10$

Table 4.3: Muon identification cuts used in this analysis.

4.7 Missing Transverse Energy

The neutrinos arising from leptonic W boson decay do not interact in the detectors. Their presence can be inferred from the imbalance of momentum in the transverse plane, called missing transverse energy (E_T^{miss}).

The missing transverse energy is constructed from the vector sum of all calorimeter cells resolved onto the transverse plane. Cells not associated to muon, electron ($p_{\mathrm{T}} > 10$ GeV), photon, τ lepton candidates and jets are included at the EM scale. The electrons, muons and jets used in the E_T^{miss} calculation are used consistently with the definitions as stated above. Photon and τ lepton candidates are also included in the E_T^{miss} calculation.

4.8 Event quality cuts

To ensure that the event was actually triggered by the leptons used in the analysis, an $\eta - \phi$ match between one of the reconstructed and selected lepton candidates and the trigger object is required. The matching distance is $\Delta R < 0.15$. After the trigger

selection, events must have an offline-reconstructed primary vertex with at least five tracks. Events are discarded if any jet with $p_T > 20$ GeV fails jet quality cuts designed to reject jets arising from out-of-time activity or calorimeter noise.

4.9 Selection of $t\bar{t}$ Events

The dilepton $t\bar{t}$ final state is characterized by two isolated lepton candidates, missing transverse energy and two b-quark jets. The selection of a dilepton candidate sample consists of a series of kinematic requirements taking advantage of these characteristics.

After the lepton selections, the primary backgrounds to $t\bar{t}$ dilepton final states are Z/γ^*+jets events. The selection cuts effective to reject this source of background events are cuts on $E_{\mathrm{T}}^{\mathrm{miss}}$, the invariant dilepton mass $m(l^+l^-)$ and the scalar transverse energy sum (H_{T}) of the selected leptons and jets. The cut on the invariant mass is only applied to the ee and $\mu\mu$ channels whereas the H_{T} cut is only applied to $e\mu$ candidates instead of the $E_{\mathrm{T}}^{\mathrm{miss}}$ cut. The cut on $m(l^+l^-)$ is applied as a veto on events in a symmetric mass window around the Z boson mass. This is usually referred as the 'Z-window' cut. In addition to these cuts, the leptons are required to be oppositely-charged and the event has to have at least two jets.

These requirements are optimized using MC samples [50]. The figure of merit for the optimization is the significance of the measurement, defined as

$$S = \frac{N_{\mathrm{S}}}{\sqrt{(\delta N_{\mathrm{stat}})^2 + (\delta N_{\mathrm{sys}})^2 + \Sigma(\delta N^i_{\mathrm{B,stat}})^2}} \tag{4.1}$$

where $N_{\mathrm{S/B}}$ is the number of signal and background events, respectively. The denominator terms are the statistical uncertainty $\delta N_{\mathrm{stat}} = \sqrt{N_{\mathrm{S}} + N_{\mathrm{B}}}$, the systematic uncertainties δN_{sys}, and the statistical uncertainty on the background prediction $\delta N^i_{\mathrm{B,stat}}$ for each background i. The systematic uncertainties include jet, lepton energy scale uncertainties and

lepton resolution uncertainties. The uncertainties are determined by shifting the energy scales and resolutions within their uncertainties, recalculating E_T^{miss} and H_T accordingly and measuring the change in the accepted number of signal and background events.

In the ee and $\mu\mu$ channels, the $E_{\mathrm{T}}^{\mathrm{miss}}$ and Z-window cuts are the most powerful in terms of improving the significance. Figure 4.2 and Figure 4.3 show the significance as a function of the Z-window when $E_{\mathrm{T}}^{\mathrm{miss}}$ is fixed at its optimum value in the ee and $\mu\mu$ channels, respectively. The significance curves shown in Figures 4.2 and 4.3 do not fall steeply from the maxima and for simplicity the same cut values of the ee and $\mu\mu$ channels were used: $E_{\mathrm{T}}^{\mathrm{miss}} > 40$ GeV and the 'Z-window' with a full width of 20 GeV (81-101 GeV) in the signal region.

Previous studies [51] had shown that a cut on $E_{\mathrm{T}}^{\mathrm{miss}}$ was not needed for the $e\mu$ channel in the presence of a H_{T} cut. So for the $e\mu$ channel only a one-dimensional optimization of H_{T} was needed, and the optimal value of $H_{\mathrm{T}} > 130$ GeV was chosen.

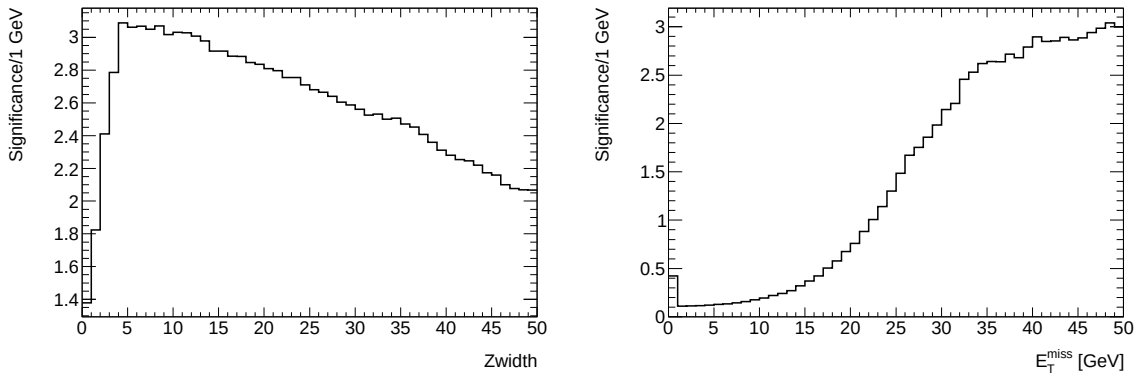

Figure 4.2: Projection of the significance vs. the Z-window cut (left) and vs. $E_{\mathrm{T}}^{\mathrm{miss}}$ (right) for the ee channel with $E_{\mathrm{T}}^{\mathrm{miss}}$ or the Z-window cut fixed at its optimized value, respectively.

Table 4.4 summarizes the selection criteria for the $t\bar{t}$ dilepton events.

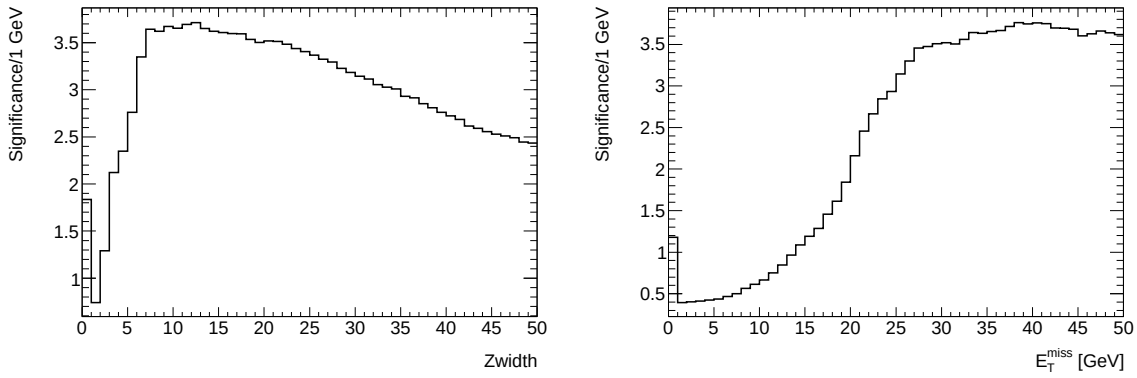

Figure 4.3: Projection of the significance vs. Z-window cut (left) and vs. $E_{\mathrm{T}}^{\mathrm{miss}}$ (right) for the $\mu\mu$ channel with $E_{\mathrm{T}}^{\mathrm{miss}}$ or the Z-window cut held at its optimized value, respectively.

cut	ee	$\mu\mu$	$e\mu$
Lepton requirement	exactly 2 leptons, $p_T > 20$ GeV		
Sign requirement	opposite signed		
Electron/muon overlap	reject event if electron and muon (before removed by jet overlap) share a track		
Cosmic rejection	muons (before removed by jet overlap): opposite signed d_0, both muons $\lvert d_0\rvert > 0.5$ mm, $\Delta\varphi > 3.10$		
Z-window	10 GeV	10 GeV	–
$E_{\mathrm{T}}^{\mathrm{miss}}/H_{\mathrm{T}}$	$E_{\mathrm{T}}^{\mathrm{miss}} > 40$ GeV	$E_{\mathrm{T}}^{\mathrm{miss}} > 40$ GeV	$H_{\mathrm{T}} > 130$ GeV
Trigger matching	lepton: match trigger $\Delta R < 0.15$, event: at least one match		
Jet req.	at least 2 jets, $\lvert\eta\rvert < 2.5$, $p_T > 20$ GeV		
Event quality	Jet cleaning cuts Number of tracks in primary vertex > 4		
Truth matching	match from MCTruthClassifier to lepton from W boson		

Table 4.4: Summary of the event selection requirements. The cuts on $E_{\mathrm{T}}^{\mathrm{miss}}$, H_{T} and 'Z-window' have been optimized in Section 4.9. The other cuts are described from Section 4.3 to Section 4.8.

Chapter 5

Background Determination and Observed Event Yields

The background rates are estimated using data whenever possible to minimize the reliance on Monte Carlo simulations. There are three categories of background sources. One is the background from Drell-Yan processes ($Z/\gamma^* \to \ell^+\ell^-$) produced with associated jets and large $E_{\mathrm{T}}^{\mathrm{miss}}$ due to resolutions effects and measurement errors. The Drell-Yan process $Z/\gamma^* \to l^+l^-$ (only here $l = e, \mu$) is the main background source of the ee and $\mu\mu$ channels, while $Z/\gamma^* \to \tau^+\tau^-$ is a significant background source for the $e\mu$ channel. An additional source of background events are from processes that contain misidentified leptons, or non-isolated lepton that are not from W decay. This type of background is known generically as the fake lepton background, and includes events with W bosons, produced in association with jets, and QCD multi-jet events. Other background sources are electroweak processes including two leptons in the decay, namely single top and diboson (WW, ZZ and WZ) production processes. The contribution from these sources are small and they are determined from Monte Carlo simulations.

The Drell-Yan backgrounds ($Z/\gamma^* \to \ell^+\ell^-$) and fake lepton backgrounds are determined using data. The methods to estimate these backgrounds and the results are

described in the following sections. The $Z \to \tau^+\tau^-$ background kinematics and normalization are taken from Monte Carlo simulations.

5.1 Drell-Yan Background

The $t\bar{t}$ event selection is designed to reject Z/γ^*+jets events. However, a small fraction of such events with large $E_{\mathrm{T}}^{\mathrm{miss}}$ and dilepton invariant mass away from the Z boson mass peak will remain in the signal sample. These events are difficult to properly model in simulations due to large uncertainties on the non-Gaussian $E_{\mathrm{T}}^{\mathrm{miss}}$ tails, on the Z boson cross section for higher jet multiplicities, and on the lepton energy resolution.

To estimate the Z/γ^*+jets background, the number of Z/γ^*+jets events is measured in a control region orthogonal to the $t\bar{t}$ dilepton signal region. The control region (CR) is formed by events with an invariant dilepton mass inside the Z mass window used in the event selection described above, with at least two jets and with $E_{\mathrm{T}}^{\mathrm{miss}} > 30$ GeV. There is contamination in the control region from other physics processes and their contribution is subtracted using the Monte Carlo predictions. A scale factor is derived using Z/γ^*+jets simulation to extrapolate from the control region into the signal region:

$$\mathrm{N}_{\mathrm{Z}/\gamma^*+\mathrm{jets}} = \frac{\mathrm{MC}_{\mathrm{Z}/\gamma^*+\mathrm{jets}}(\mathrm{SR})}{\mathrm{MC}_{\mathrm{Z}/\gamma^*+\mathrm{jets}}(\mathrm{CR})} \times (\mathrm{Data}(\mathrm{CR}) - \mathrm{MC}_{\mathrm{other}}(\mathrm{CR}))\,, \tag{5.1}$$

where $\mathrm{MC}_{\mathrm{Z}/\gamma^*+\mathrm{jets}}(\mathrm{SR/CR})$ represent the number of events in the signal and control region, respectively. The variable $\mathrm{MC}_{\mathrm{other}}$ is the number of events from other physics backgrounds that contaminate the control region, while Data(CR) represents the observed number of events in the control region.

The robustness of the method is tested by varying the $E_{\mathrm{T}}^{\mathrm{miss}}$ cut in the control region by ± 5 GeV, and the resulting variation in background rates is referred to as the 'method uncertainty'. The comparison between data-driven and Monte Carlo methods demonstrates that the data-driven normalization using the control regions helps to re-

Process	ee	$\mu\mu$
Z/γ^*+jets (data-driven)	$1.2^{+0.5}_{-0.6}$	$3.4^{+1.9}_{-1.4}$
Z/γ^*+jets (Monte Carlo)	$2.8^{+3.1}_{-1.8}$	$3.4^{+4.1}_{-2.4}$

Table 5.1: Yields and total uncertainties for the estimates of the Z/γ^*+jets background with data-driven and Monte Carlo methods.

duce the systematic uncertainties. The number of Z/γ^*+jets background events from this data-driven method is summarized in Table 5.1 for the ee and $\mu\mu$ channels. The most important uncertainties on the estimation are shown in Table 5.2 for the ee and $\mu\mu$ channel, respectively.

Uncertainty(%)	ee (DD)	ee (MC)	$\mu\mu$ (DD)	$\mu\mu$ (MC)
Data statistics	+34/-27	-	+14/-13	-
Jet energy scale	+8/-16	+104/-51	-23/+45	+114/-57
Jet energy resolution	±7	±22	±6	±13
Monte Carlo cross section	-4/+7	±29	+4/-9	±38
Monte Carlo statistics	±18	±17	±15	±15
Muon momentum resolution	-	-	+3/-5	+3/-5
Method (see text)	±27	-	±22	-
total (syst + lumi + stat)	±46	+112/-66	+56/-41	+122/-72

Table 5.2: Dominant (and total) uncertainties on the predicted number of Z/γ^*+jets events in the signal region from data statistics, jet energy scale, jet energy resolution, theoretical MC cross sections, MC statistics and lepton energy resolutions. The uncertainty due to the method is evaluated from the variation of the prediction when the $E_{\mathrm{T}}^{\mathrm{miss}}$ cut in the control region is varied by ±5 GeV. The uncertainties are compared between the data-driven (DD) determination and the determination from Monte-Carlo simulations. The uncertainties of the prediction are presented as +1 σ / -1 σ variations.

5.2 Fake lepton Backgrounds

True $t\bar{t}$ dilepton events contain two leptons from W decays. The background comes predominantly from W+jets events (including the single lepton $t\bar{t}$ production) with one real and one fake lepton, though there is a smaller contribution arising from events with two fake leptons coming from QCD multi-jet production. In the case of muons, the

dominant fake-lepton mechanism is the semi-leptonic decay of a heavy-flavour hadron, in which a muon survives the isolation requirement. In the case of electrons, the three mechanisms to produce false candidates are heavy flavour decay, light flavour jets with a leading π^0 overlapping with a charged particle, and conversion of photons[1].

The fraction of the dilepton sample that comes from fake leptons is measured with a matrix method. 'Loose' muons are defined in the same way as tight muons (see Section 4.6), except that the calorimeter and track isolation are relaxed. 'Loose' electrons must fulfill the tight electron cuts described in Section 4.4, except that the requirements on calorimeter isolation, high threshold TRT hits and on E/p are relaxed [45].

The loose lepton selection criteria are then applied to the event sample and we count the number of observed dilepton events with two tight, two loose or one tight and one loose leptons (N_{TT}, N_{LL} or N_{TL} and N_{LT}, respectively). Then two probabilities are defined, r (f), to be the probability that real (fake) leptons that pass the loose identification criteria, will also pass the tight criteria. Using r and f, linear expressions are then obtained for the observed yields as a function of the number of events with two real, two fake or one real and one fake leptons (N_{RR}, N_{FF} and N_{RF} or N_{FR}, respectively). The method explicitly accounts for the presence of events with two fake leptons. These linear expressions form a matrix that is inverted in order to extract the real and fake content of the observed dilepton event sample:

$$\begin{bmatrix} N_{TT} \\ N_{TL} \\ N_{LT} \\ N_{LL} \end{bmatrix} = \begin{bmatrix} rr & rf & fr & ff \\ r(1-r) & r(1-f) & f(1-r) & f(1-f) \\ (1-r)r & (1-r)f & (1-f)r & (1-f)f \\ (1-r)(1-r) & (1-r)(1-f) & (1-f)(1-r) & (1-f)(1-f) \end{bmatrix} \begin{bmatrix} N_{RR} \\ N_{RF} \\ N_{FR} \\ N_{FF} \end{bmatrix} \tag{5.2}$$

[1]The latter process generates a real electron, but for convenience we include it in the fake lepton category

Fake lepton background	N_{jets}	$e\mu$	ee	$\mu\mu$
Matrix method	0	$1.9 \pm 1.0 \pm 1.0$	$1.4 \pm 0.8 \pm 0.7$	$0.0\,^{+0.6}_{-0} \pm 0.3$
Matrix method	1	$3.9 \pm 1.5 \pm 2.0$	$1.9 \pm 0.9 \pm 1.0$	$0.0\,^{+0.6}_{-0} \pm 0.3$
Matrix method	≥ 2	$3.0 \pm 2.1 \pm 1.5$	$0.8 \pm 0.7 \pm 0.4$	$0.5 \pm 0.5 \pm 0.3$
Candidate weighting	≥ 2	$1.1 \pm 0.6^{+0.3}_{-0.2}$	$0.6 \pm 0.3^{+0}_{-0.1}$	$2.2 \pm 1.1^{+0}_{-0.2}$

Table 5.3: Overview of the estimated fake lepton background yields in the signal and control regions using the matrix method. In the signal region ($N_{\text{jets}} \geq 2$) the method is cross-checked with the candidate weighting method. The matrix method is used as a baseline since it includes contributions from events with two fake leptons, and is less sensitive to potential trigger and $E_{\text{T}}^{\text{miss}}$ bias. Statistical and systematic uncertainties are shown.

The efficiency for a real loose lepton to pass the tight criteria, r, is measured in data in a sample of $Z \to \ell\ell$ events as a function of jet multiplicity. The corresponding efficiency for fake leptons, f, is measured in data in events with a single loose lepton and low $E_{\text{T}}^{\text{miss}}$, which are dominated by QCD di-jet production. Contributions from real leptons due to W+jets final states are subtracted using simulated data.

A cross-check of these results comes from comparing results of the matrix method with the 'candidate weighting method'. Isolated tracks (loose electrons) are used as muon (electron) candidates. The rates at which these candidates are identified as muons (electrons) are measured in the inclusive $W \to \mu\nu$ sample. Events are selected to contain at least one muon and at least one isolated track candidate, and to have $E_{\text{T}}^{\text{miss}} > 20$ GeV. To suppress dileptons from Z/γ^*+jets events, the muon and candidate within a pair are required to have the same charge. Known sources of same-sign leptons are subtracted using MC. To estimate the non-Z background, the obtained rates are then applied to the sample containing exactly one good lepton and at least one additional candidate lepton. The dominant uncertainties are due to data statistics.

Table 5.3 shows the background estimates obtained from the matrix and candidate weighting methods. The two methods are found to agree on the estimated background within their uncertainties.

5.3 Other Backgrounds

The contributions from other small cross section electroweak background processes, such as single top and dibosons are estimated according to Monte Carlo prediction. The expected number of background events from a process is calculated by

$$N_{expected} = \mathcal{L} \times \sigma_{process} \times \frac{N_{pass}}{N_{total}}, \tag{5.3}$$

where $\mathcal{L}$ is the integrated luminosity (35 pb^{-1} in this analysis); $\sigma_{process}$ is the theoretical cross section of a given process, the acceptance $A = \frac{N_{pass}}{N_{total}}$ is a ratio of events which pass the selection criteria discussed in Chapter 4. This ratio is calculated using Monte Carlo simulations.

The systematic uncertainties from the MC-based backgrounds includes the uncertainties on the integrated luminosity, the theoretical cross sections and the object identification, which will be discussed in detail in Chapter 8.

5.4 Control Regions

The modeled signal selection acceptance and background contributions are validated by comparing Monte Carlo simulations with data in control regions which are depleted of $t\bar{t}$ events, but have similar kinematics. In particular, the Z mass region, defined as $|m(l^+l^-) - m_Z| \leq 10$ GeV is used for the ee and $\mu\mu$ samples.

Figure 5.1 (a) and (d) show the $E_{\mathrm{T}}^{\mathrm{miss}}$ distribution for events in the Z boson mass region and requiring at least 2 jets, (b) and (e) show the jet multiplicity for events where the dilepton mass lies inside the Z boson peak and $E_{\mathrm{T}}^{\mathrm{miss}} < 40$ GeV. This tests the initial state radiation (ISR) modeling of jets for the Drell-Yan processes. The dilepton mass plots, Figure 5.1 (c) and (f), probe the modeling of the lepton energy scale and resolution.

In general good agreement between the background model and the data is observed.

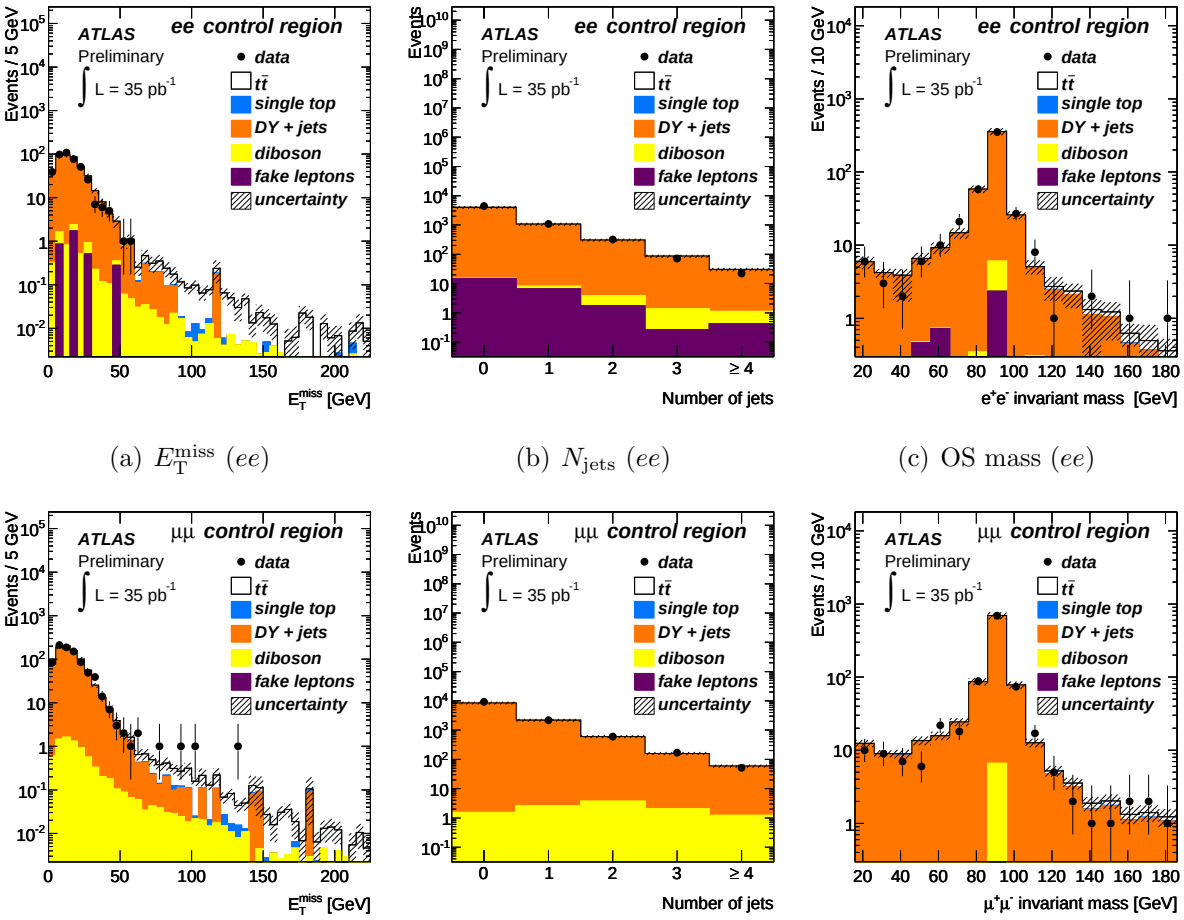

(a) $E_{\mathrm{T}}^{\mathrm{miss}}$ (ee) (b) N_{jets} (ee) (c) OS mass (ee)

(d) $E_{\mathrm{T}}^{\mathrm{miss}}$ $(\mu\mu)$ (e) N_{jets} $(\mu\mu)$ (f) OS mass $(\mu\mu)$

Figure 5.1: Top row ee, bottom row $\mu\mu$: (a),(d) $E_{\mathrm{T}}^{\mathrm{miss}}$ in events with a dilepton mass inside the Z mass window with $\geq$ 2 jets, (b),(e) the number of jets in events with a dilepton mass inside the Z mass window and $E_{\mathrm{T}}^{\mathrm{miss}}$ < 40 GeV and (c),(f), the invariant mass of opposite-sign lepton pairs in events with $\geq$2 jets in the low $E_{\mathrm{T}}^{\mathrm{miss}}$ region. The error bands reflect the statistical and systematic uncertainties of the MC prediction.

5.5 Signal Regions

The expected and measured numbers of events in the signal region after applying all selection cuts as described in Chapter 4 for each of the individual dilepton channels are shown in Table 5.4. In the data set of $\mathcal{L}$=35 pb^{-1} a total of 105 candidate events are

observed, 16 in the ee-channel, 31 in the $\mu\mu$-channel and 58 in the $e\mu$-channeł.

	ee	$\mu\mu$	$e\mu$
Z+jets (DD)	$1.2^{+0.5}_{-0.6}$	$3.4^{+1.9}_{-1.4}$	-
$Z(\rightarrow \tau\tau)$+jets (MC)	$0.4^{+0.4}_{-0.3}$	$1.2^{+0.7}_{-0.6}$	$3.2^{+1.6}_{-1.3}$
Non-Z leptons (DD)	0.8 ± 0.8	0.5 ± 0.6	3.0 ± 2.6
Single top (MC)	0.7 ± 0.1	1.3 ± 0.2	2.5 ± 0.4
Dibosons (MC)	0.5 ± 0.1	0.9 ± 0.2	$2.1^{+0.5}_{-0.3}$
Total (non $t\bar{t}$)	3.5 ± 1.1	$7.3^{+1.8}_{-1.5}$	10.8 ± 3.4
$t\bar{t}$ (MC)	11.5 ± 1.3	20.1 ± 1.7	47.4 ± 4.0
Total expected events	15.0 ± 1.7	27.4 ± 2.4	58.2 ± 5.2
Observed events	16	31	58

Table 5.4: The full breakdown of the expected $t\bar{t}$-signal and background in the signal region compared to the observed event yields, for each of the dilepton channels (MC is simulation based, DD is data driven). All systematic uncertainties are included and the correlation between the different background sources are taken into account.

In Figure 5.2, the distributions of the number of selected jets are shown for ee, $\mu\mu$ and $e\mu$ channels together with the expectation for $\mathcal{L}$=35 pb^{-1} from Monte-Carlo simulation and data-driven methods, after applying all requirements except for the jet multiplicity cut. The $E_{\mathrm{T}}^{\mathrm{miss}}$ distributions for the ee and $\mu\mu$ channels and the H_{T} distribution for the $e\mu$ channel are shown in Figure 5.3. Finally, in Figure 5.4 the distribution of the number of jets are shown for all dilepton channels combined. All of these distributions are in good agreement with the expected background rates and ttbar signal.

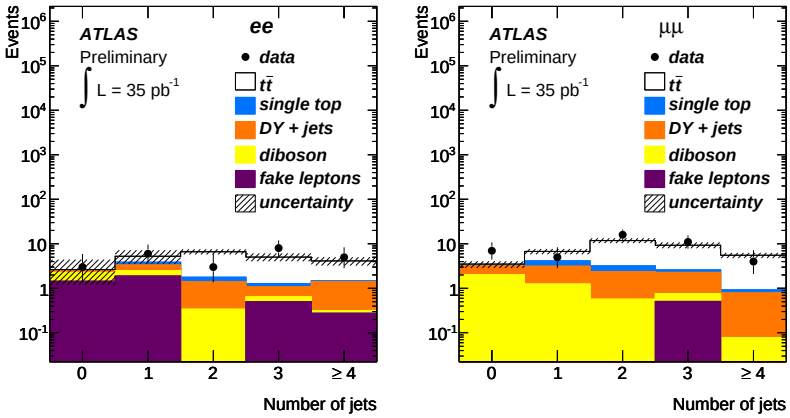

(a)

(b)

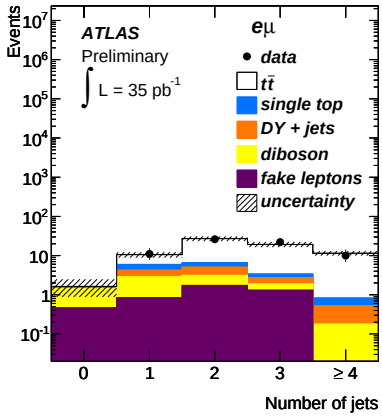

(c)

Figure 5.2: Jet multiplicities for the signal region omitting the $N_{\text{jets}} \geq 2$ requirement in (a) the ee channel, (b) the $\mu\mu$ channel and (c) the $e\mu$ channel.

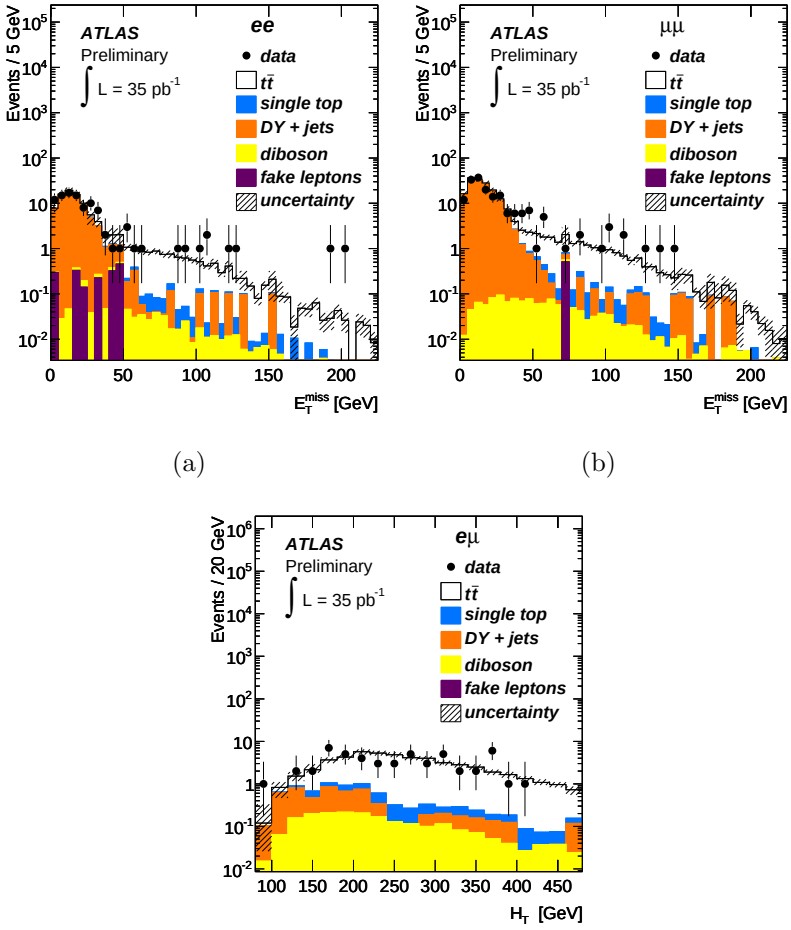

Figure 5.3: The $E_{\mathrm{T}}^{\mathrm{miss}}$ distribution in the signal region for (a) the ee channel and for (b) the $\mu\mu$ channel without the $E_{\mathrm{T}}^{\mathrm{miss}} > 40$ GeV requirement, and (c) the distribution of the H_{T}, defined as the scalar sum of the transverse energies of the two leptons and all selected jets, in the signal region without the $H_{\mathrm{T}} > 130$ GeV requirement.

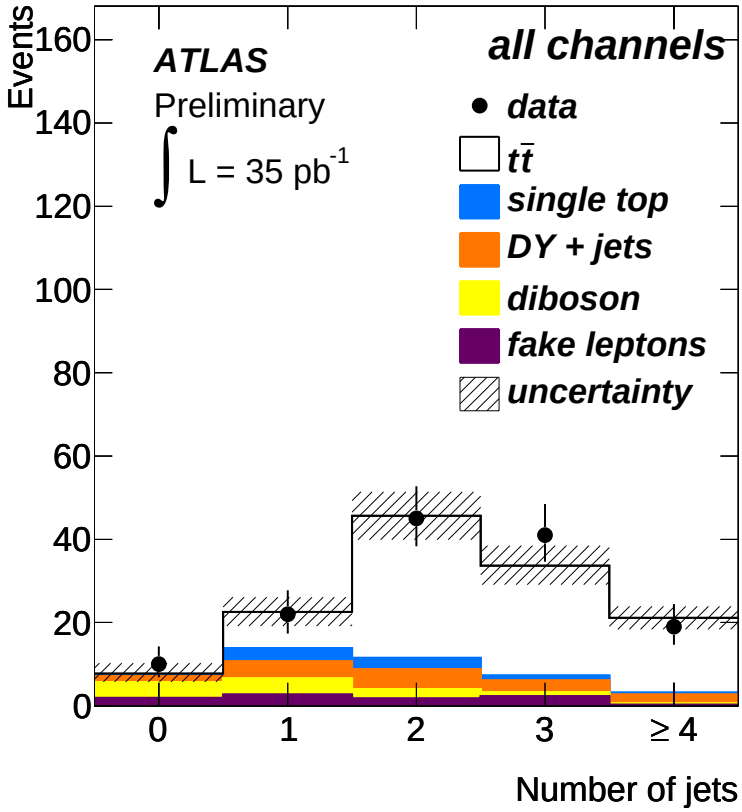

Figure 5.4: Jet multiplicity in the signal region without the $N_{\text{jets}} \geq 2$ requirement for the combined dilepton channels.

Chapter 6

b-Quark Jet Tagging

Many physics analyses at ATLAS rely on the identification of jets containing b-quarks. The discrimination of b-quark jets from light quark jets originates mainly in the relatively long lifetime of b-hadrons, resulting in a significant flight path length. This leads to measurable secondary vertices and impact parameters of the decay products, as shown in Figure 6.1. The transverse and longitudinal impact parameters d_0 and z_0 are defined as the transverse (r/ϕ-projection) and $z-$coordinate of a track at the point of closest approach of the track to the primary vertex, respectively.

It is also possible to identify a b-jet using "soft-lepton" tagging, where one takes advantage of the property that the decay of B hadrons give rise to leptons (e or μ) 40% of the time. Several "soft-lepton" b-tagging algorithms have been developed for ATLAS [5], but they are not used in this analysis.

6.1 b-tagging Performance Estimators

6.1.1 Jet Flavor Labeling

For b-tagging purposes, the direction of the jet is used to define which tracks should be associated with the jet. The actual tagging is done on this subset of tracks. Tracks within

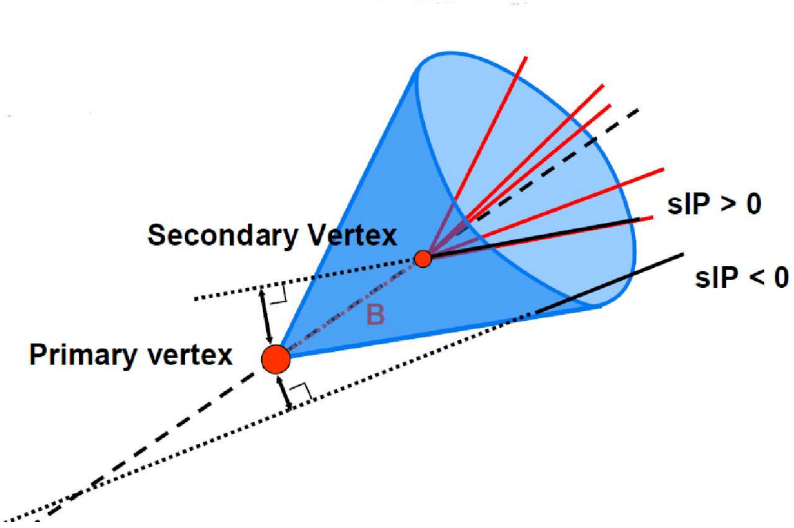

Figure 6.1: Illustration of the displaced vertex and impact parameter of a b-quark jet.

a distance $\Delta R < 0.4$ of the jet axis are associated to the jet. A given track is associated to the jet that is the closest in ΔR to it. The jet direction is also used to determine the sign of the impact parameters of the tracks in the jet. The impact parameter is positive if the angle between the jet direction and the perpendicular joining the primary vertex and the position of closest approach of the track is less than 90°, negative otherwise, as illustrated in Figure 6.1.

To measure and compare the b-tagging performance with the one predicted by ATLAS detector simulation, one needs to be able to label the jet flavour in the MC samples. The MC event history is used to know the type of parton from which a jet originates. This labeling procedure is not unambiguous and it not strictly identical for different MC generators. For the results presented in the ATLAS flavour tagging studies, a ΔR quark labeling has been used [52]: a jet is labeled as a b-jet if a b-quark with $p_T > 5$ GeV is found in a cone of size $\Delta R = 0.3$ around the jet direction. The labeling hypotheses are tried in this order: b-quark, c-quark, and τ lepton. When no heavy flavour quark nor τ lepton satisfies these requirements, the jet is labeled as a light-jet. No attempt is made to distinguish between u, d, s quarks and gluons since such a label is even more ambiguous

and not relevant for this study.

6.1.2 Efficiency and Rejection

For performance studies, only jets fulfilling the requirement that $p_T > 15$ GeV and $|\eta| < 2.5$ are deemed taggable and considered. In the studies carried out in this thesis, we applied $p_T > 20$ GeV and $|\eta| < 2.5$ for the jets. Therefore all of the jets are taggable in the selected samples.

The tagging efficiency, ϵ_b, is naturally defined as the fraction of taggable jets labeled as b-jets which are actually tagged as b-jets by the tagging algorithm under study. The mis-tagging efficiencies, ϵ_c and ϵ_l, for charm and light quark jets, are the fraction of taggable jets labeled as c-jets and light quark jets which are mistakenly tagged as b-jets. The light jet rejection is usually used instead of the mis-tagging efficiency, which is simply the inverse of the mis-tagging efficiency. The definitions of the tagging efficiency and rejections are shown in Equations 6.1.

$$\begin{aligned} \epsilon_b = \frac{N_b^{tagged}}{N_b}, \quad \epsilon_c = \frac{N_c^{tagged}}{N_c}, \quad \epsilon_l = \frac{N_l^{tagged}}{N_l}, \\ R_c = \frac{1}{\epsilon_c}, \quad R_l = \frac{1}{\epsilon_l}. \end{aligned} \tag{6.1}$$

6.2 The b-tagging Algorithms

In this section, the various algorithms used in ATLAS to tag b-jets are described. The spatial algorithms, built on tracks and subsequently vertices, are the most powerful ones. Soft lepton tagging algorithms are also important, in particular since the correlation with the spatial algorithms is minimal, although they aren't used explicitly in this analysis.

6.2.1 JetProb

A simple but robust approach to select b-jets makes use of the signed impact parameter significance d_0/σ_{d_0} of each track associated with the jet in question. It compares this to a resolution function $\mathcal{R}$ for prompt tracks to measure the probability $\mathcal{P}_i$ that the track i has its origin at the primary vertex known as JetProb tagger [5]. The individual probability, $\mathcal{P}_i$, is

$$\mathcal{P}_i = \int_{-\infty}^{-|d_0^i/\sigma_{d_0}^i|} \mathcal{R}_i \, dx \tag{6.2}$$

The probability for each of the N_T tracks associated to the jet are then combined to obtain a jet specific discrimination probability $\mathcal{P}_{\text{jet}}$

$$\begin{aligned} \mathcal{P}_{\text{jet}} &= \mathcal{P}_0 \sum_{j=0}^{N_T-1} \frac{(-\ln \mathcal{P}_0)^j}{j!} \\ \mathcal{P}_0 &= \prod_{i=1}^{N_T} \mathcal{P}_i' \qquad \text{where} \quad \begin{cases} \mathcal{P}_i = \frac{\mathcal{P}_i}{2} & \text{if } d_0^i > 0 \\ \mathcal{P}_i = \left(1 - \frac{\mathcal{P}_i}{2}\right) & \text{if } d_0^i < 0 \end{cases}, \end{aligned} \tag{6.3}$$

To discriminate b-jets from c-jets and light quark jets, the b-weight is derived from the logarithm of the probability ($W_{\text{JP}} = -\ln \mathcal{P}_{\text{jet}}$). Since $\mathcal{P}_{\text{jet}}$ indicates the probability of a light-quark jet, W_{JP} is increasing with the probability for b-jets. The efficiencies and rejections for the JetProb tagger are shown in Figure 6.2. In contrast to the other taggers, the weights of the JetProb tagger are by construction only positive. This tagger is of high importance due to its robustness for commissioning and for cross-checks with other taggers. Furthermore, the JetProb tagger was also designed to provide high-efficiency operating points up to $\epsilon_b \approx 80$ %.

6.2.2 SV0

The SV0 tagger [5, 53] is based on the lifetime measurement by the explicit reconstruction of secondary vertices from tracks associated with the jet in question. Within a given

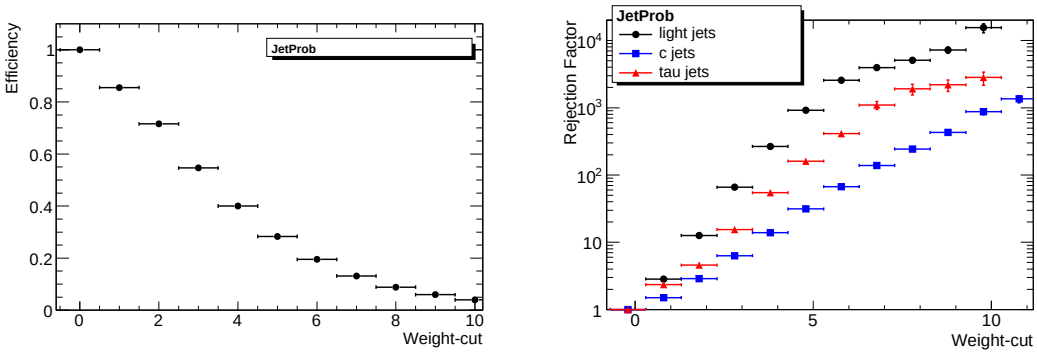

Figure 6.2: The efficiency (left) and rejection (right) of the JetProb tagger, obtained using MC@NLO $t\bar{t}$ MC simulation. The jets are AntiKt4TopoJets, required to have $p_T > 15$ GeV and $|\eta| < 2.5$.

jet, the two-track vertices that are significantly displaced from the primary vertex are reconstructed. Those that are consistent with K^0_S or Λ^0 decays, $\gamma \to e^+e^-$ conversions, or material interactions are removed. A secondary vertex fit is performed on the remaining tracks, iteratively removing the track with the highest contribution to the χ^2 until an acceptable χ^2 is obtained. The weight is the three-dimensional signed decay length significance, $L/\sigma(L)$, of the secondary vertex position with respect to the primary vertex. The sign is given by the sign of the projection of the decay length vector on the jet axis. The efficiencies and rejections for the SV0 tagger are shown in Figure 6.3.

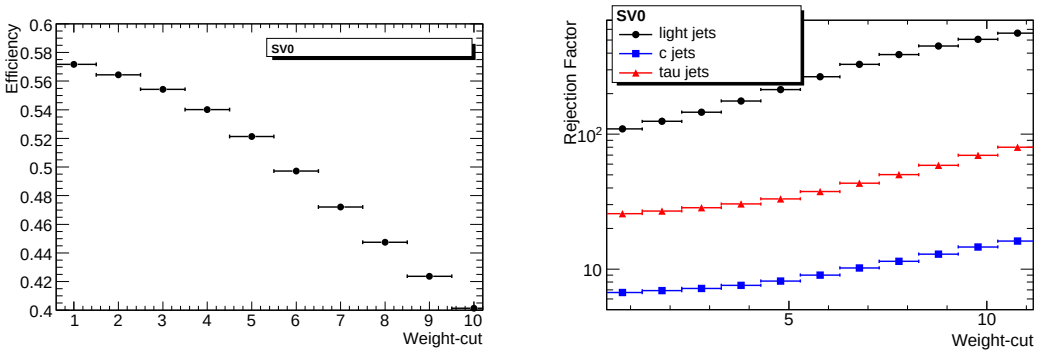

Figure 6.3: The efficiency (left) and rejection (right) of the SV0 tagger, obtained using MC@NLO $t\bar{t}$ MC simulation. The jets are AntiKt4TopoJets, required to have $p_T > 15$ GeV and $|\eta| < 2.5$.

6.2.3 IP3D+SV1

The weight for the IP3D+SV1 tagger [5] is a sum of the individual weights of the SV1 and IP3D taggers. Both of these taggers rely on creating likelihood ratios for a measured discriminating variable, S_i, within the selected jet that are compared to predefined reference probability distributions $u(S_i)$ for light jets and $b(S_i)$ for b-jets. The reference probability distributions are obtained from Monte Carlo calculation. The ratio of the probabilities $b(S_i)/u(S_i)$ defines the track or vertex weight, which can be combined into a jet weight W_{jet} by forming a logarithmic sum of the N_T tracks within the jet.

SV1 is a secondary vertex tagger that forms a likelihood ratio using distributions of the mass of tracks in the vertex and the ratio of the summed energies of tracks in the vertex. IP3D is an impact parameter based tagger, which uses 2-dimensional histograms of the longitudinal versus transverse impact parameters to form a likelihood ratio for each track. The tracks in the jet are combined to make a jet weight. The efficiencies and rejections for the IP3D+SV1 tagger are shown in Figure 6.4.

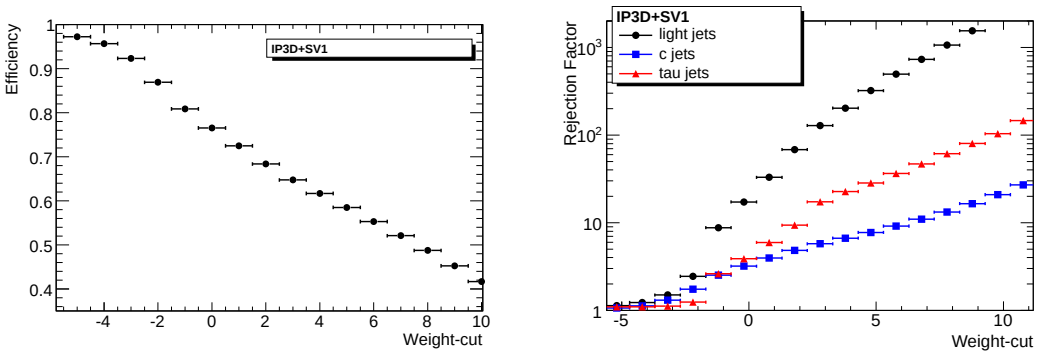

Figure 6.4: The weight distribution (left), and rejection (right) of the IP3DSV1 tagger, obtained using MC@NLO $t\bar{t}$ MC simulation. The jets are AntiKt4TopoJets, required to have $p_T > 15$ GeV and $|\eta| < 2.5$.

6.2.4 JetFitterComb

The JetFitter tagger is a b-tagging algorithm making use of a vertexing algorithm which attempts to reconstruct the vertex combination of PrimaryVertex $\rightarrow B \rightarrow D$ decay chain in a single pass, making only the assumption that the decay vertices of the weakly decaying B/D hadrons lie on the same "flight axis". The tag weight is defined as the logarithm of probabilities $\log(Prob(b-\text{jet})/Prob(\text{light}-\text{jet}))$. For JetFitterComb, which is the combination of IP3D and JetFitter tagging weights, a simple addition of the log likelihood values is made, taking advantage the fact that the secondary vertex and impact parameter based likelihood functions are largely uncorrelated. The efficiencies and rejections for the JetFitterComb tagger are shown in Figure 6.5.

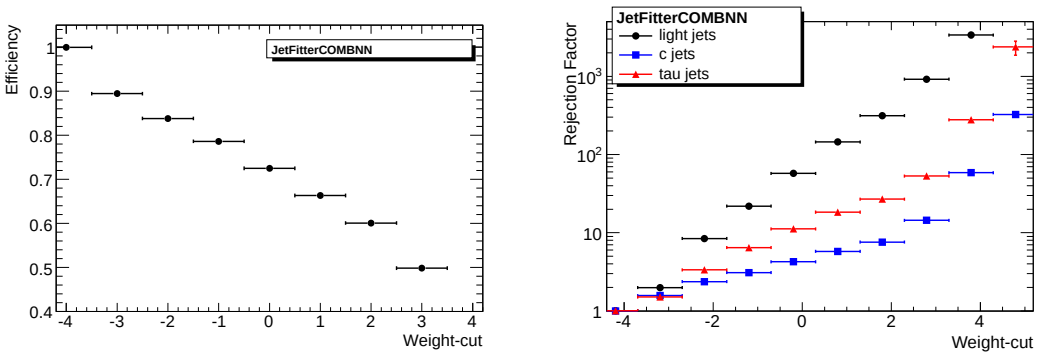

Figure 6.5: The weight distribution (left), and rejection (right) of the JetFitterComb tagger, obtained using MC@NLO $t\bar{t}$ MC simulation. The jets are AntiKt4TopoJets, required to have $p_T > 15$ GeV and $|\eta| < 2.5$.

6.2.5 Soft Lepton Algorithms

Soft lepton tagging relies on the semi-leptonic decays of bottom and charm hadrons. Therefore it is intrinsically limited by the branching ratios to leptons: about 20% of b-jets will contain a soft lepton of a given flavour, including cascade decays of bottom to charm hadrons. However, tagging algorithms based on soft leptons exhibit very high purity and low correlations with the track-based tagging algorithms, which is very important

for checking and cross-calibrating performance in data. Once a reconstructed muon or electron is associated to a jet, a likelihood discriminates light jets from b-jets. A light jet rejection of about 300 can be achieved for a b-tagging efficiency of 10% for the soft muon tagging algorithm, and a light jet rejection of about 100 can be achieved for a b-tagging efficiency of 7% with the soft electron tagging algorithm. The primary limitations are the low efficiencies of the algorithms.

6.3 The b-tagging Working Points

A comparison of the taggers described above is given in Figure 6.6 for light jets and c-jets, where the rejection as a function of the tagging efficiency is presented. IP3D+SV1 and JetFitter are sophisticated taggers which have the best performance, a light rejection of 1000 can be reached for tagging efficiency around 50%. However, they depend on combinations of various discriminating variables and need special data-driven calibration of the inputs to the algorithms. The SV0 and JetProb tagging algorithms are simple and robust b-tagging algorithms. In contrast to the other lifetime taggers no a-priori knowledge of the properties of either b-jets or light jets is necessary. Therefore, these taggers are particularly well suited for early data and have been used by the ATLAS collaboration for the analyses that observed top quark production at the LHC [31].

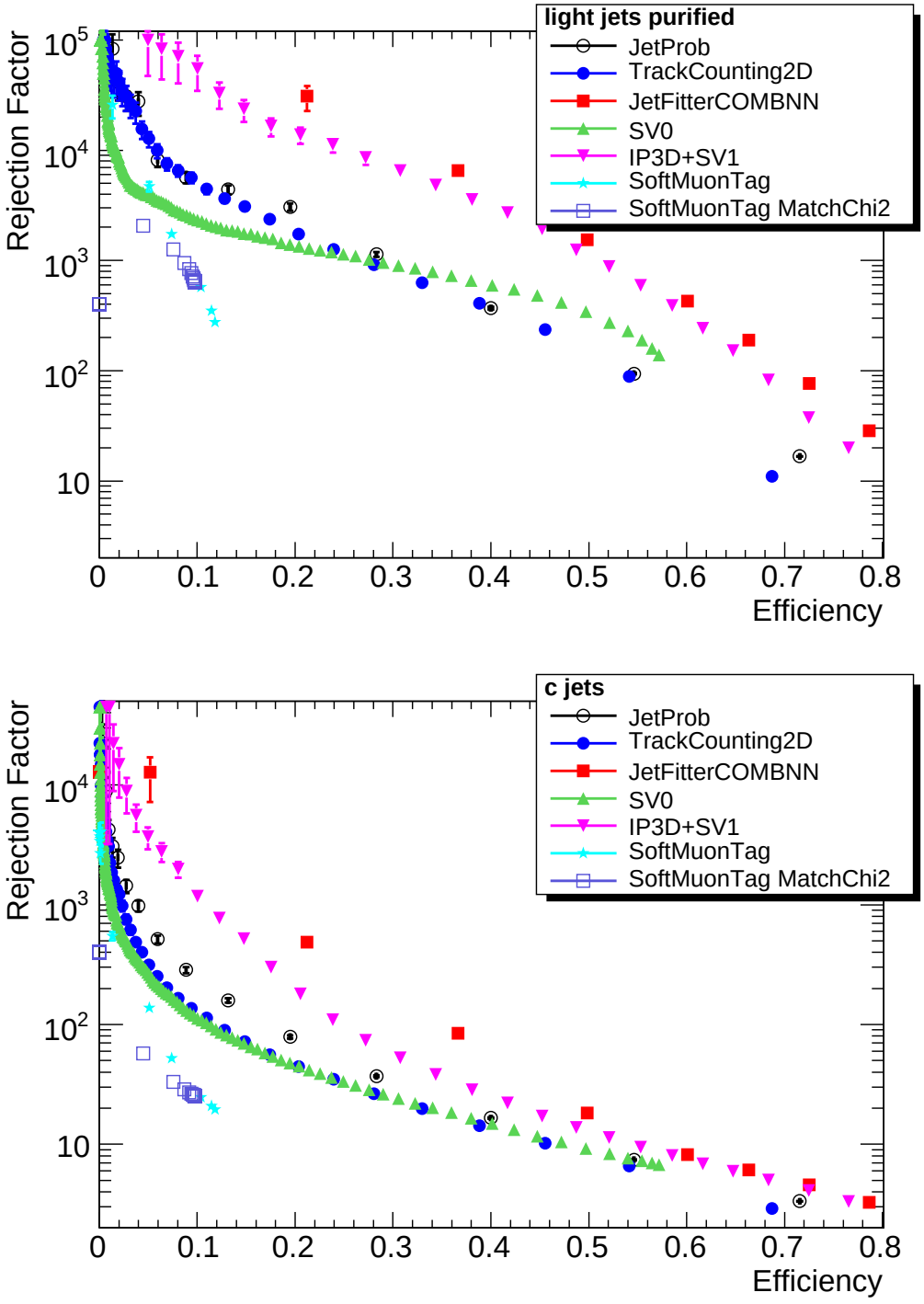

Figure 6.6: Comparison of the rejection rates as a function of b-tagging efficiency for the TrackCounting, JetProb, SV0, IP3D+SV1, JetFitterComb, Soft Muon and χ^2_{match}/DoF taggers for light jets (upper) and c-jets (lower).

Chapter 7

The Tag Counting Method

At the beginning of LHC data taking, the performance of the b-tagging algorithms has to be understood using data. The Tevatron experiments (CDF and D0) have developed methods to measure the b-tagging efficiency with dijet events and inclusive lepton sample. At the LHC, the large $t\bar{t}$ production cross-section and lower relative background rates offer an alternative calibration tool to determine the b-tagging efficiency.

In-situ b-tagging calibration with dileptonic $t\bar{t}$ events offers several advantages:

- The heavy flavor content of dilepton $t\bar{t}$ events is relatively well-known. With the two top quarks decaying to Wb, as discussed in Section 2.2.3, the $t\bar{t}$ pair gives rise to two b-jets, the leptonic decays of W bosons produce two high-p_T leptons and missing transverse energy. Additional jets from ISR and FSR cause some confusion and introduce systematic uncertainties, which are discussed later in the thesis.

- The environment of large jet multiplicity and the typically high p_T b-jets in $t\bar{t}$ events are taken into account since the measurement uses the same $t\bar{t}$ data sample.

- The distinctive topology of two oppositely charge leptons, two b-jets and missing transverse energy is relatively easy to trigger and isolate, as discussed in Chapters 4 and 5.

The calibration technique discussed in this thesis is based on dileptonic $t\bar{t}$ events where we count the number of events with different number of b-tagged jets (the tag counting method).

7.1 The Maximum Likelihood Fit

The tag counting method assumes that there is no correlation between b-tags within an event, while the multi-jet environment may affect the vertex reconstruction and introduce such a correlation. This assumption was checked by selecting MC events with two reconstructed b-jets in the detector acceptance. The correlation in the efficiency of tagging two b-jets is quantified by the covariance

$$cov(tag_1, tag_2) = \frac{N^{2b-tags}}{N} - \epsilon_b^2, \tag{7.1}$$

where $N^{2b-tags}$ is the number of events with two tagged b-jets, N is the total number of events, and ϵ_b is the b-tagging efficiency. It was found that the covariance is of order 10^{-4}, which is consistent with zero for our purposes [54].

In a simplified case, we assume every selected event contains two b-jets in the detector acceptance and that only b-jets can be tagged. Then it is clear that the expected number of events with one b-tagged jet is proportional to $N2\epsilon_b(1-\epsilon_b)$, while the expected number of events with two b-tagged jets is proportional to $N\epsilon_b^2$, where:

- ϵ_b is the average b-tagging efficiency, i.e. the probability to tag a b-jet; and
- N is the the number of selected $t\bar{t}$ events prior to any b-tagging requirement, which is proportional to the $t\bar{t}$ production cross-section, the event selection efficiency and the integrated luminosity, $N = L \cdot \sigma_{t\bar{t}} \cdot \epsilon_{pre-tag}$.

The b-tagging efficiency can be derived from the ratio of the observed numbers of events with one and two b-tagged jets.

In reality, c-jets and light jets are present and contribute to the number of tagged jets in the event. Moreover, not all b-jets coming from the top quark decays end up being selected, whilst a number of b-jet candidates are produced through gluon radiation. Taking these effects into account, the expected number of events with n b-tagged jets, $< N_n >$, can be written as:

$$< N_n >= \sum_{i,j,k} \Big\{ [\sigma_{t\bar{t}} \cdot BR \cdot A_{t\bar{t}} \cdot Lumi \cdot F^{t\bar{t}}_{i,j,k} + N_{Z+jets} F^{Z+jets}_{i,j,k} + N_{other} \cdot F^{other}_{ijk}] \times \sum_{i'+j'+k'=n} C^{i'}_{i} \epsilon_b^{i'} (1-\epsilon_b)^{i-i'} \cdot C^{j'}_{j} \epsilon_c^{j'} (1-\epsilon_c)^{j-j'} \cdot C^{k'}_{k} \epsilon_l^{k'} (1-\epsilon_l)^{k-k'} \Big\}, \quad (7.2)$$

where $\sigma_{t\bar{t}}$ is the $t\bar{t}$ production cross section, BR is the branching ratio to each final state (ee, $\mu\mu$ and $e\mu$) and $A_{t\bar{t}}$ is the selection efficiency in this final state, i, j and k (i', j' and k') are the number of pretagged (tagged) b-, c- and light-flavour jets and $C^{\alpha'}_{\alpha}$ is the number of permutations $\frac{\alpha!}{\alpha'! \cdot (\alpha - \alpha')!}$ with $\alpha = i, j, k$ for the three jet flavours. The parameters N_{Z+jets} and N_{other} are the expected number of background events in each final state. We separate the Z+jets events from the other backgrounds since this is the dominant background in the ee and $\mu\mu$ channels and can be readily measured. Other background contributions are fixed to the Monte Carlo values for single top and diboson backgrounds and to the data driven estimates for the fake lepton background. The flavour fractions, $F_{i,j,k}$, are estimated for both $t\bar{t}$ signal and background events using MC simulation, the dominant contributions for the $F_{i,j,k}$ values in the $\mu\mu$ channel are shown in Table 7.1. As expected, the $t\bar{t}$ signal events are heavy-flavour dominated while the Z+jets background is light flavour dominated.

The expected number of events in each b-tagged jet multiplicity bin is fitted to the observed distribution with the following likelihood function:

F_{ijk}	$t\bar{t}$	F_{ijk}	Z+Jets
F_{200}	30.9±0.4%	F_{002}	40.3±0.5%
F_{201}	26.2±0.4%	F_{003}	24.5±0.4%
F_{202}	11.8±0.3%	F_{004}	14.8±0.3%
F_{101}	11.4±0.3%	F_{005}	5.3±0.2%
F_{102}	6.0±0.2%	F_{011}	3.2±0.2%
F_{203}	4.4±0.2%	F_{012}	2.3±0.1%
F_{204}	1.2±0.1%	F_{101}	0.4±0.1%

Table 7.1: Flavour composition of selected $t\bar{t}$ candidate events for the signal events and Z+jets background events. Only the dominate contributions are shown to illustrate the difference between the two type of events. These values rely on labeling of jet flavour in the MC simulations. This is done by a standard jet-parton matching algorithm in ATLAS, which labels the jet flavour by a ΔR matching between jet and the truth partons in the MC generator. A default $\Delta R = 0.3$ cone size is used in the labeling algorithm consistently for both the F_{ijk} values and the MC b-tagging efficiency calculation. The uncertainty on these F_{ijk} values arise from how well the MC simulation models the flavour compositions, and will be discussed in Section 7.2.

$$L = \prod_{ee,\mu\mu,e\mu} \text{Gaus}(N_Z; N_Z^0, \delta N_Z^0) \times \prod_{\text{bins}} [\text{Pois}(N_n^{obs}, < N_n >)]\Big\}, \tag{7.3}$$

where $< N_n >$ is the expected number of events with n b-tagged jets, and N_n^{obs} is the observed number from the data, as shown in Figure 7.1. Since the background contribution is relatively low in the dilepton channel, the fitting also includes the zero tag bin. The fitting parameters in the likelihood function are the b-tagging efficiency and the $t\bar{t}$ cross section. The number of Z+jets background events in each channel are also fitting parameters which are constrained to the results from data driven estimations as discussed in Section 5.1. As shown in Equation 7.3, N_Z is the fitting parameter of number of Z+jets events in each channel, N_Z^0 and δN_Z^0 are the estimated number of Z+jets events and the uncertainty of the estimation, respectively. The event selection acceptance and branching ratio are fixed inputs in the likelihood function, whose values are listed in Table 7.2 and Table 7.3, respectively.

	ee	$\mu\mu$	$e\mu$
Acceptance	0.117	0.205	0.243

Table 7.2: Selection acceptance in the $t\bar{t}$ signal sample with the event selection cuts described in Section 4.9. MC@NL0+HERWIG MC sample is used to calculate the acceptance.

	ee	$\mu\mu$	$e\mu$
BR (%)	1.67	1.64	3.40

Table 7.3: Branching ratio for $t\bar{t}$ events to decay to dilepton final states. The intermediate $W \to \tau \to e(\mu)$ decay is also taken into account.

7.2 Fitting Results with SV0 Tagging Algorithm

After the event selections discussed in Chapter 4, the SV0 b-tagging algorithm at a weight cut of 5.85, which corresponds to a b-tagging efficiency of about 50%, is applied to the candidate $t\bar{t}$ dilepton events. The observed b-tagged jets multiplicity distributions are shown in Figure 7.1, superimposed with the expected distributions from MC simulations.

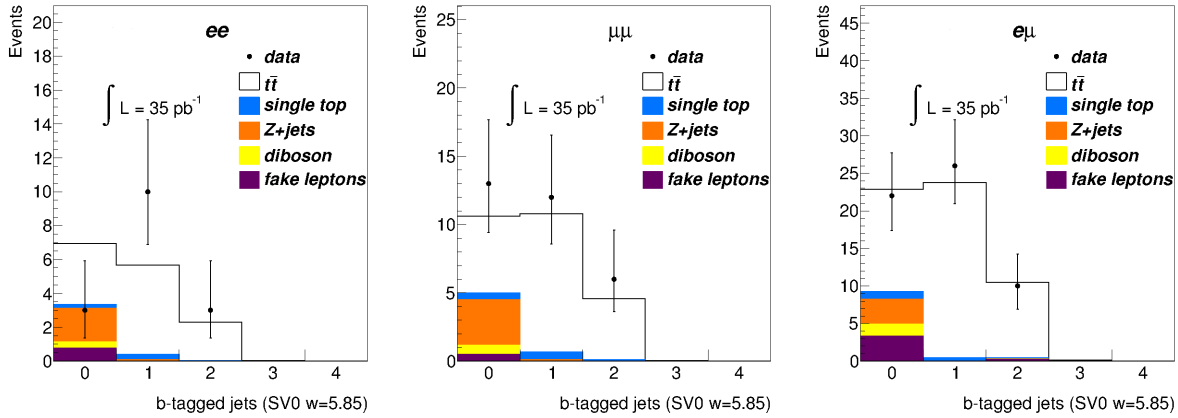

Figure 7.1: The distribution of the number of b-tagged jets distribution in the ee, $\mu\mu$ and $e\mu$ channels, with the "SV0" b-tagging algorithm at the working point corresponding to a nominal 50% b-tagging efficiency.

The maximum likelihood fitting described in Section 7.1 is applied to the observed b-tagged jet multiplicity distribution, shown in Figure 7.1. The fitting parameters are

the b-tagging efficiency (ϵ_b) and $t\bar{t}$ cross section ($\sigma_{t\bar{t}}$). The log-likelihood in Equation 7.3 as a function of these two parameters is shown in Figure 7.2. The values that maximize (and thus minimizes the negative of the log likelihood) the likelihood in Equation 7.3 are the fit results.

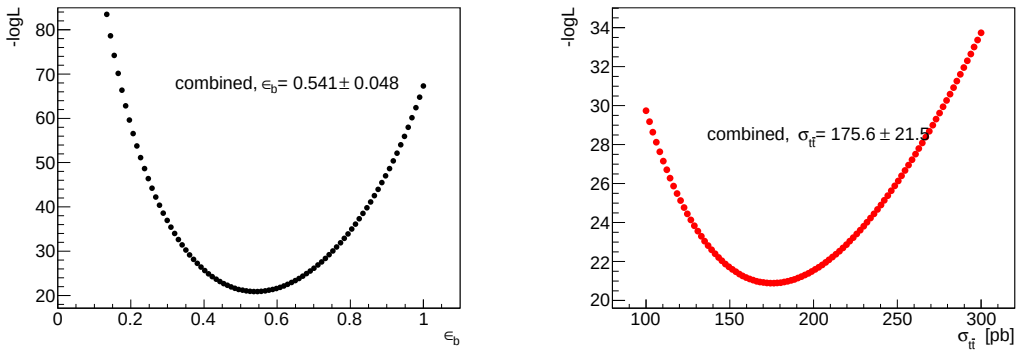

Figure 7.2: The log likelihood as a function of the fitting parameters ϵ_b (left) and $\sigma_{t\bar{t}}$ (right). The b-tagging working point used is "SV0" tagging algorithm at weight cut 5.85, which corresponds to b-tagging efficiency of 50%.

The fitted b-tagged jet multiplicity distribution and the 2D contour of the fitting result for the b-tagging efficiency and the $t\bar{t}$ cross section are shown in Figure 7.3. The uncertainties on the 2D contour plot include the data statistics. The measured value of the b-tagging efficiency is in agreement with the MC simulation, and the $t\bar{t}$ cross-section agrees with MC@NLO prediction within one standard deviation.

7.3 Consistency Checks

We check that the likelihood fit described above yields unbiased results by sampling the MC data set and repeating the fitting. This procedure of creating ensembles of "pseudo-experiments" is commonly used to identify any biases and verify the statistical validity of the technique. The pseudo-experiments are generated in the following manner:

- The expected number of signal and background events are randomly sampled from

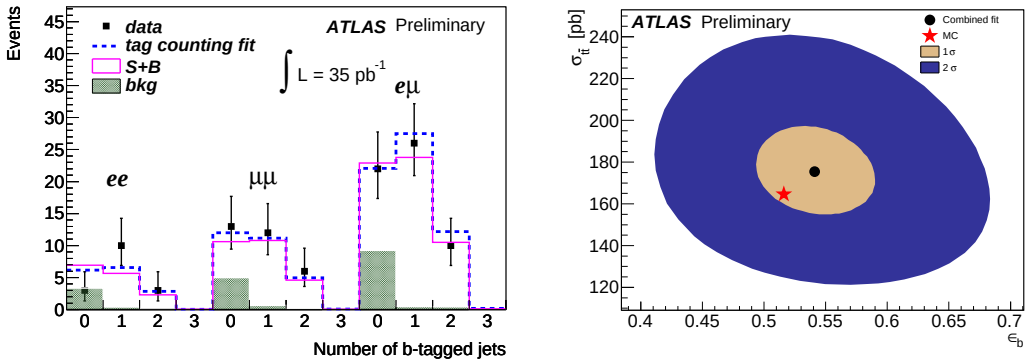

Figure 7.3: Fitted b-tagged jet multiplicity distribution superimposed with the observed distribution (left) and 2D contour for the measured b-tagging efficiency and $t\bar{t}$ cross section when combining the ee, $\mu\mu$ and $e\mu$ final states (right). Only statistical uncertainties are included in the plots. The b-tagging working point used is the SV0 tagging algorithm with a weight cut of 5.85, which corresponds to a nominal b-tagging efficiency of 50%.

large MC data sets. The number of events in each process corresponds to the theoretical cross section multiplied by the integrated luminosity.

- The sampled events are passed through the event selection for $t\bar{t}$ dilepton as described in Chapter 4. The b-tagging algorithm is applied to the events that pass the selection.

- The maximum likelihood fit described above is applied to the resulting b-tag jet multiplicity distribution.

- The above procedure is repeated multiple times and each repetition is one pseudo-experiment. The distributions of fit results for ϵ_b and σ_{tt} are used to check the consistency of the maximum likelihood fitting.

The pulls for ϵ_b and $\sigma_{t\bar{t}}$ are defined as $(\epsilon_b^{fit} - \epsilon_b^{MC})/\delta\epsilon_b$ and $(\sigma_{t\bar{t}}^{fit} - \sigma_{t\bar{t}}^{MC})/\delta\sigma_{t\bar{t}}$, respectively, where ϵ_b^{fit} and ϵ_b^{MC} are the fitting results and expected values from Monte-Carlo, respectively, and $\delta\epsilon_b$ is the expected statistical uncertainty from the fit. Similarly, $\sigma_{t\bar{t}}^{fit}$, $\sigma_{t\bar{t}}^{MC}$, and $\delta\sigma_{t\bar{t}}$ are the fitted cross section, theoretical cross section and statistical uncertainty, respectively.

Figure 7.4 shows the pull distributions of ϵ_b and $\sigma_{t\bar{t}}$ from 1000 pseudo-experiments, fitted with Gaussian distributions. As expected, the mean of the distribution is centered at zero, and the width of the distributions are consistent with unity. This confirms that the maximum likelihood fitting is unbiased and correctly estimates the statistical uncertainties.

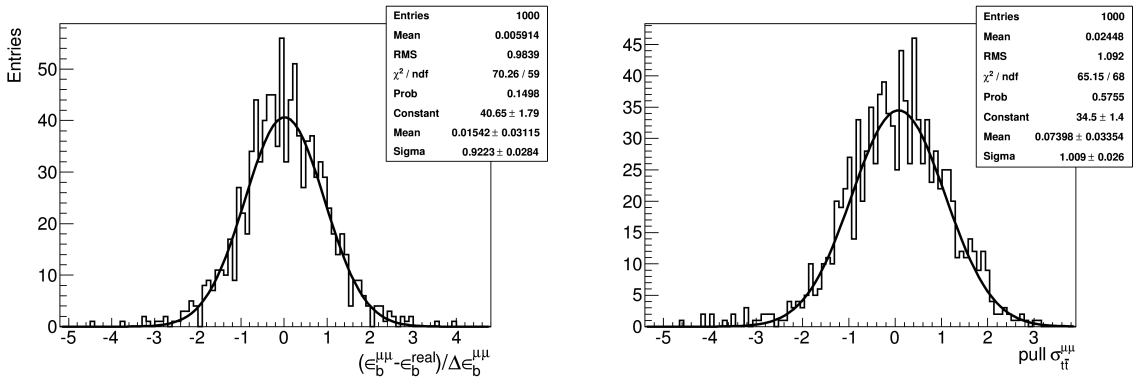

Figure 7.4: Pull distribution for ϵ_b (left) and $\sigma_{t\bar{t}}$ (right) with 1000 pseudo-experiments. The b-tagging working point used is the SV0 tagging algorithm at weight cut 5.85, which corresponds to b-tagging efficiency of 50%.

As a cross-check, another way of generating the pseudo-experiments is to randomly fluctuate the number of events per bin in the b-tagged jets multiplicity distribution using a Poisson distribution, where the expected value in each bin is calculated with large Monte-Carlo samples of signal and background events. The fluctuation procedure is repeated multiple times and the same distributions for the two fitting parameters are produced. This way of generating the pseudo-experiments gives rise to the same conclusion, as above, that the fitting results are unbiased.

We check that the fitting is unbiased over the full range of the fit parameters by varying the input values of the $t\bar{t}$ cross section away from the theoretical values and look at the fitted results for ϵ_b and $\sigma_{t\bar{t}}$. The results are shown in Figure 7.5. The fit results for $\sigma_{t\bar{t}}$ are consistent with the input cross sections, and ϵ_b remains unchanged, as expected.

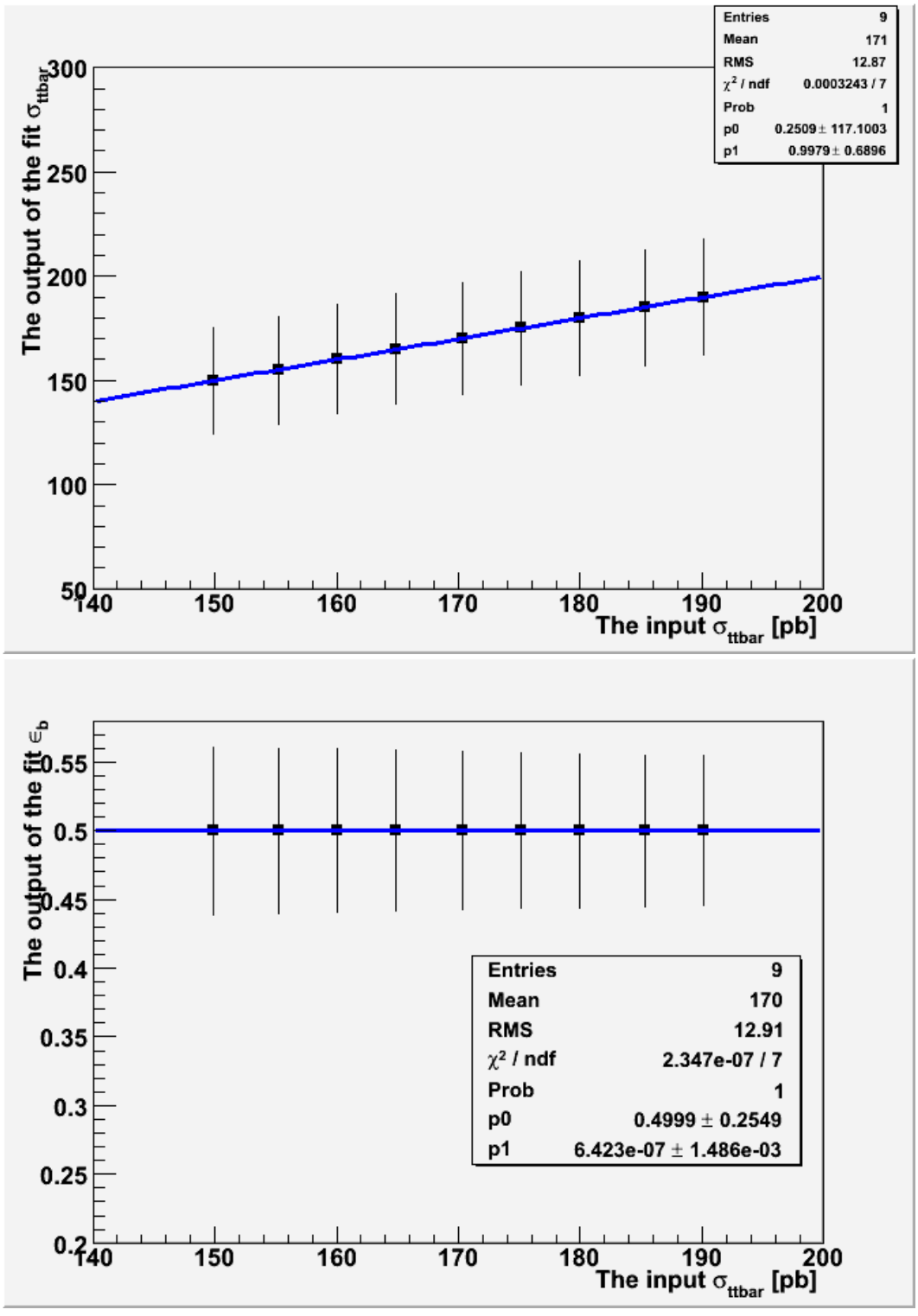

Figure 7.5: The output from the likelihood fitting for $\sigma_{t\bar{t}}$ (upper) and ϵ_b (lower) as a function of input $\sigma_{t\bar{t}}$. The statistical uncertainty of the fitting results are shown.

Chapter 8

Results and Systematic Uncertainties

Various effects can influence the fitting results for the b-tagging efficiency and $t\bar{t}$ cross section, including MC modeling of the physics processes, detector effects and the uncertainty introduced by the data-driven estimation of background processes. All these effects have been investigated and their contributions to the measurement uncertainties will be outlined in this chapter.

8.1 Signal Generator

The use of simulated $t\bar{t}$ samples to calculate the signal acceptance gives rise to systematic uncertainties from the choice of generator. Various samples have been generated to assess these effects. As discussed in Section 4.2, the Monte Carlo samples generated by MC@NLO interfaced with HERWIG is used as the baseline sample in this analysis. The positive weight emission generator (POWHEG) [55] also produces final states at next-to-leading-order accuracy and enables valuable systematic studies to the generator uncertainty. The comparison has been made between MC@NLO+HERWIG and POWHEG+HERWIG samples, and the differences are taken as the systematic uncertainty

due to the MC generator.

In order to study the effect of different models for hadronisation, both HERWIG and PYTHIA were used to hadronise POWHEG samples. The difference between POWHEG+HERWIG and POWHEG+PYTHIA samples was used to estimate the systematic uncertainty due to hadronisation models. The choice of the three $t\bar{t}$ signal samples, MC@NLO+HERWIG, POWHEG+HERWIG, and POWHEG+PYTHIA makes it is possible to separate the effects of event generation and hadronisation models.

8.2 Parton Distribution Uncertainty

The systematic uncertainty due to the parton distribution functions (PDF) is evaluated on the $t\bar{t}$ signal samples using the envelope of error bands from CTEQ66, MSTW08 [56] and NNPDF2.0 [57] sets. In order to avoid generating a sample for each source of PDF uncertainty, a re-weighting method has been used [58]. The selection efficiencies for the re-weighted samples have been compared with the nominal $t\bar{t}$ signal sample and the difference is taken as the systematic uncertainty due to the uncertainties in the PDFs.

8.3 Initial and Final State Radiation

More initial and final state QCD radiation (ISR and FSR) increases the number of jets and affects the transverse momentum of particles in the event. Selection cuts for top quark events are sensitive to the number and kinematics of the jets, and so ISR and FSR will have some effect on the selection efficiency. In order to evaluate the uncertainties arising from ISR and FSR, the AcerMC generator [59] interfaced with PYTHIA is used. The PYTHIA parameters related to ISR and FSR are varied in a range consistent with experimental data [60]. The parameters varied to increase and decrease the ISR and FSR are given in Table 8.1. The uncertainties from ISR and ISR are estimated by taking the difference between the ISR/FSR varied samples and the baseline sample.

Parameter	ISR ↓ value	ISR ↑ value	Baseline	FSR ↓ value	FSR ↑ value
PARP(64)	4.0	0.25	1.0	1.0	1.0
PARP(67)	0.5	6.0	1.0	1.0	1.0
PARP(72) [GeV]	0.192	0.192	0.192	0.092	0.384
PARJ(82) [GeV]	1.0	1.0	1.0	2.0	0.5

Table 8.1: Parameter variations in Pythia used for ISR and FSR samples.

8.4 Pile-up Uncertainty

Pile-up effects result in additional energy deposits that affect not only the jet reconstruction, but also the $E_{\mathrm{T}}^{\mathrm{miss}}$ in an event which is an important discrimination variable for the analysis. The simulation included effects from pile-up by overlaying randomly minimum bias events to achieve a certain average number of vertices.

Figure 8.1 shows the number of reconstructed vertices in events with an invariant dilepton mass around the Z mass. The vertices are required to have more than 4 tracks and must be identified as a primary or pile-up vertex. It can be seen that in both ee and $\mu\mu$ channels the MC has pile-up events with a higher average number of vertices.

A reweighting method according to the number vertices observed in the event sample has been adopted for MC events. The weights are consistent between ee and $\mu\mu$ events. The effect of the reweighting is checked by comparing the $E_{\mathrm{T}}^{\mathrm{miss}}$ distribution of data and Monte-Carlo before and after reweighting, as shown in Figure 8.2.

The same comparison of the $E_{\mathrm{T}}^{\mathrm{miss}}$ distribution for events within the Z boson mass window, but with high jet multiplicity shows good agreement between data and MC, regardless of the reweighting, as it can be seen in Figure 8.3. A similar level of agreement can be seen for $\mu\mu$ events. Hence the samples used in this analysis are not reweighted and the change of the analysis with pile-up reweighting can be used as a systematic uncertainty.

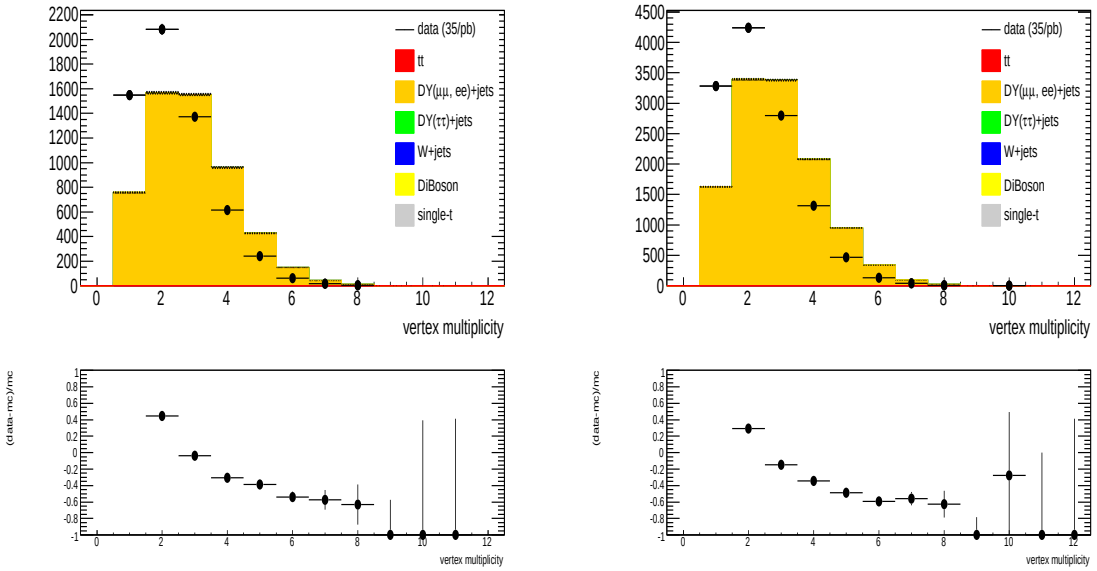

Figure 8.1: Number of reconstructed vertices in the ee channel (left) and the $\mu\mu$ channel (right) in the Z enhanced region. The observed data is shown with the black dots and MC distribution is shown in filled histograms. The bottom panels show the difference between data and MC.

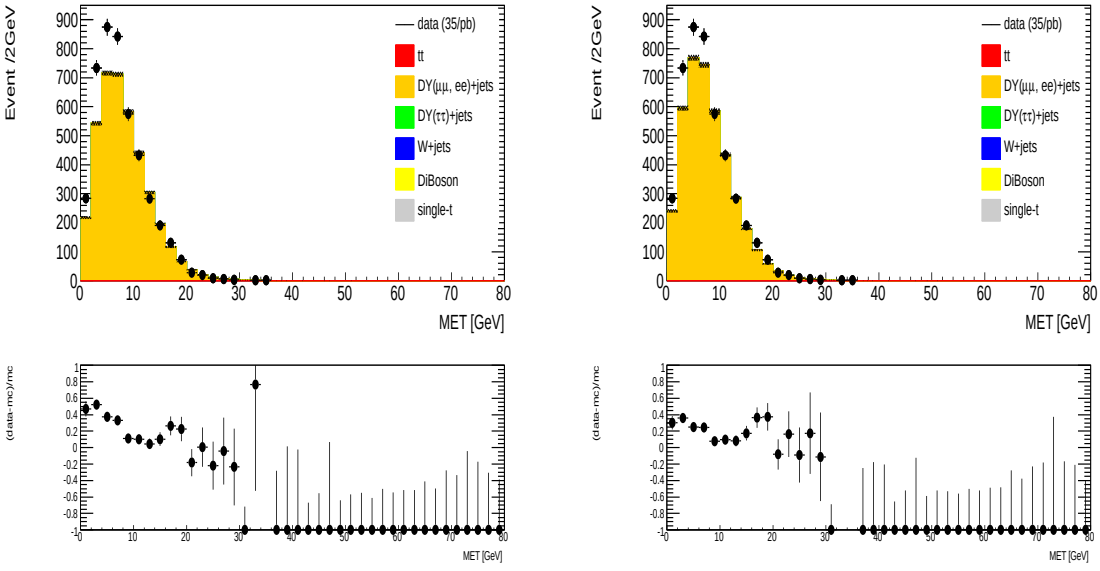

Figure 8.2: The $E_{\mathrm{T}}^{\mathrm{miss}}$distributions for the $Z \to ee$ candidate sample with zero jets before (left) and after (right) reweighting.

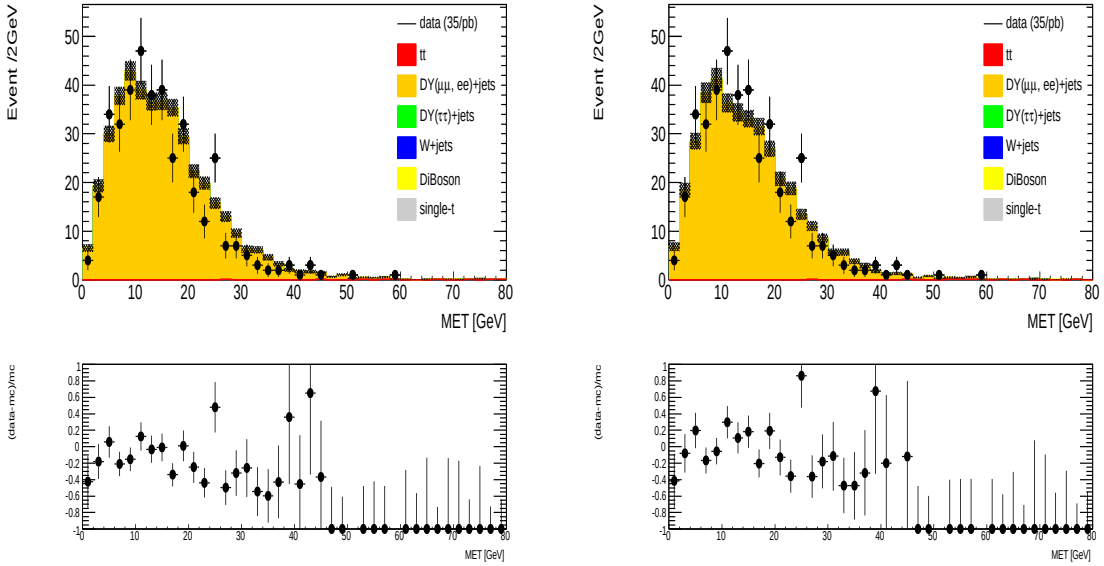

Figure 8.3: The $E_{\mathrm{T}}^{\mathrm{miss}}$distributions for the $Z \to ee$ candidate sample with 2 or more jets before (left) and after (right) reweighting in the ee channel.

8.5 Lepton Reconstruction Uncertainty

The uncertainties due to Monte Carlo simulation modeling of the lepton trigger, reconstruction and selection efficiencies have been assessed using tag and probe techniques, where one lepton candidate is used to tag the event and the second is used as a probe in the events consistent with Z boson decays. This technique is applied to $Z \to$ ee and $Z \to \mu\mu$ events selected from the same data sample as used for the $t\bar{t}$ analyses. Lepton trigger, reconstruction and identification efficiencies in simulation were found to be consistent with data within 1% [45].

8.6 Jet Energy Scale

The jet energy scale (JES) and its uncertainty has been derived combining information from test-beam data, LHC collision data and simulation [61], and the uncertainty varies in the range 4–6% as a function of jet p_T and η.[1] Effects from nearby jets are also taken

[1]The `MultijetJESUncertaintyProvider` tool [62] was used to access specific uncertainty values.

into account by adding an additional 5% term to the jet energy scale uncertainty if a jet with $p_{\mathrm{T}} > 10$ GeV is within $\Delta R < 0.6$ of the nearest jet. The uncertainty on the jet energy resolution (JER) is also taken into account. It is estimated that the resolution in data and simulation agree within 14% [63]. The jet reconstruction efficiency (JEF) is reproduced by the simulation to about 2% uncertainty [48].

Jet energy scale and resolution uncertainties have been propagated into an uncertainty in $E_{\mathrm{T}}^{\mathrm{miss}}$ by re-calculating $E_{\mathrm{T}}^{\mathrm{miss}}$ once the jet energy scale have been shifted within their uncertainties to ensure the momentum of the event is balanced in the transverse plane.

8.7 Background Determination

8.7.1 Drell-Yan Background

The expected contribution from Drell-Yan production is estimated using the data-driven method described in Section 5.1. The uncertainties of the estimation is summarized in Table 5.2. We expect $1.2^{+0.5}_{-0.6}$ events to pass the dilepton selection cuts in the ee channel and $3.4^{+1.9}_{-1.4}$ events in the $\mu\mu$ channel.

8.7.2 Fake Lepton Background

The $t\bar{t}$ signal events contains two leptons from W-boson decays. Events with a jet mis-identified as a lepton or semi-leptonic decay of heavy-flavor hadrons may survive the selection cuts and contribute as backgrounds. The matrix method is used to estimate this background as discussed in Section 5.2, and the results are summarized in Table 5.3. In the signal region ($N_{jets} \geq 2$), the expected numbers of fake lepton background are 0.8 ± 0.8, 0.5 ± 0.6 and 3.0 ± 2.6 events in the ee, $\mu\mu$ and $e\mu$ channels, respectively.

8.7.3 Single Top and Diboson

The estimation of single top and diboson backgrounds relies on Monte-Carlo simulations. The overall normalization uncertainties for these two processes are taken from the theoretical uncertainties, which are 10% [64, 65] for single top and 5% [66] for diboson productions.

8.8 Flavor Composition

The flavour composition (F_{ijk} in Equation 7.2) of the pre-selected sample (see Section 4.9) relies on MC simulations. The uncertainties on the flavour composition arise from how well it is modeled by MC simulations. Specific MC samples have been generated to study this effect. We estimate the uncertainties of flavour composition by calculating the F_{ijk} values with different MC samples. For $t\bar{t}$ signal samples, we compare the baseline MC@NLO+Herwig sample with PowHeg+Herwig and PowHeg+Pythia samples. The difference between the fitting results when using the different MC calculations are taking as systematic uncertainties.

In addition, the flavour composition is also affected by ISR and FSR. The MC samples with ISR/FSR variances as described in Section 8.3 are used to study this effect. We calculate the F_{ijk} values with these ISR/FSR variant samples and compare the fitting results with the nominal one. This results 1.5% uncertainty in the measured b-tagging efficiency values and a 1% effect on the $t\bar{t}$ cross section fitting, in addition to the ISR/FSR effect on the signal acceptance.

The uncertainties on JES also affect the flavour composition by changing the selected jets sample, and thus introduce additional uncertainties in the b-tagging efficiency and $t\bar{t}$ cross section measurement. This JES effect is estimated by scaling the jet p_T by their expected uncertainties based on p_T and $|\eta|$ of the jets. We scale the jet energy and rescale the missing transverse energy before the selection, then rerun the baseline pre-selection

and calculate the F_{ijk} values with the JES variant samples. The difference between the variant and nominal cases are taken as systematic uncertainties from the JES effect on flavour composition.

8.9 Z+Heavy Flavor Fraction

The normalization on the Z+jets background is taken from the data-driven estimations, but the flavour content relies on MC simulations. The uncertainty on the Z+heavy flavour fraction is estimated by scaling the $Z + b\bar{b}$ contribution by $\pm 100\%$ from the theoretical predictions and then recalculating the flavour content in the Z+jets sample.

8.10 Charm and Light Jet Tagging

The tagging efficiencies for charm and light jets are fixed in the tag counting fitting. The values of this two parameters are taken from $t\bar{t}$ Monte Carlo samples, taking into account the scale factors measured using data-driven techniques [67]. The uncertainties of these data-driven measurement are also propagated to the uncertainties on the b-tagging efficiency and $t\bar{t}$ cross section.

8.11 Integrated Luminosity

As discussed in Section 4.1, the total integrated luminosity for the data sample is $\mathcal{L}$=35 pb^{-1} with a 3.4% uncertainty. This uncertainty propagates directly to the $t\bar{t}$ cross section measurement and is taken into account in the analysis.

8.12 Propagation of Uncertainties

8.12.1 Uncertainty of Signal Acceptance

In the case of the $t\bar{t}$ cross section measurement, uncertainties come from determining the selection acceptance ($A_{t\bar{t}}$) in the pre-selected sample. The following sources contribute to the signal acceptance uncertainties: jet energy scale; jet energy resolution; energy scale, energy resolution and object identification for electron and muon; trigger efficiency; MC generator and parton shower modeling; initial and final state radiation and the uncertainties from pile-up. Their effects on the signal acceptance are summarized in Table 8.2.

As in Equation 7.2 the uncertainty on $A_{t\bar{t}}$ propagates directly to the cross section measurement and thus makes the b-tagging efficiency measurement independent of $A_{t\bar{t}}$.

8.12.2 Nuisance Parameters

The maximum likelihood fitting method described in Section 7.1 in Equation 7.2 relies on several input parameters: the signal acceptance, the number of expected background events, the flavour composition of the events, and the mis-tag efficiencies for charm and light jets. The uncertainties of these parameter will propagate to the fitting results for the b-tagging efficiency and $t\bar{t}$ cross section. For each source of systematic uncertainty a nuisance parameter is introduced,

$$L = \prod_{ee,\mu\mu,e\mu} \prod_{j \in \text{syst}} \text{Gaus}(\alpha_j; \alpha_j^0, \sigma_j) \times \prod_{\text{bins}} \text{Pois}(N_n^{obs}, < N_n >), \tag{8.1}$$

where N_n^{obs} are the observed number of events in each b-tagged jet multiplicity bin, $< N_n >$ is the expected number of events given by Equation 7.2, j is the index of the source of systematic uncertainties, including signal acceptance, background contributions, tagging efficiencies for charm and light jets, and the integrated luminosity; α_j is the fitting

Channel	ee	$\mu\mu$	$e\mu$
Acceptance	0.117	0.205	0.243
Source of Uncertainty		$\delta A_{t\bar{t}}/A_{t\bar{t}}$ (%)	
MC Stat	±2.2	±1.6	±1.1
Pile-up	±0.9	±0.7	±0.6
JES	+6.7/-6.4	+2.7/-4.7	+2.1/-2.3
JER	±1.3	±1.0	±0.3
JEF	±1.3	±1.5	±1.6
Mu ID SF	-	+0.7/-0.7	+0.4/-0.4
Mu Trig SF	-	+0.3/-0.3	+0.0/-0.0
Electron ID SF	+5.2/-5.2	-	+3.7/-3.7
Electron Trig SF	+1.0/-1.0	-	+0.1/-0.1
Muon Energy Scale	-	+0.3/-0.3	+0.1/-0.1
Muon Resolution (MS)	-	+0.0/-0.1	+0.0/-0.0
Muon Resolution (ID)	-	+0.0/-0.0	+0.0/-0.0
Electron Energy Scale	+0.4/-0.6	-	+0.1/-0.1
Electron Resolution	+0.0/-0.1	-	+0.0/-0.0
Parton Shower	±5.5	±2.4	±4.2
Generator	±1.8	±0.4	±1.7
ISR	+4.5/-0.0	+1.6/-1.0	+3.2/-0.0
FSR	+5.3/-0.0	+7.2/-0.0	+2.5/-0.0
PDF	±2.5	±1.9	±2.2
Total	+13.1/-10.9	+8.8/-6.2	+8.0/-7.0

Table 8.2: Uncertainties on the selection acceptance ($A_{t\bar{t}}$) in the pre-selected sample. This uncertainty propagates directly to the measurement of the on $t\bar{t}$ cross section.

parameters for these uncertainties, being constrained with a Gaussian distribution with mean and width at the expected values for these sources.

We first fix these nuisance parameters at their expected values, perform the maximum likelihood fit, and obtain a set of fitting uncertainties for b-tagging efficiency and $t\bar{t}$ cross section, $\delta\epsilon_{fix}$, $\delta\sigma_{fix}$. Then the Gausain constrain for a given systematic uncertainty is introduced and the nuisance parameter is allowed to vary in the fitting. Another set of fitting results are obtained, $\delta\epsilon_{con}$ and $\delta\sigma_{con}$. The quadratic difference between the fitting results with nuisance parameter constrained and fixed is the systematic uncertainty from this given source:

$$\delta\epsilon = \sqrt{(\delta\epsilon_{con})^2 - (\delta\epsilon_{fix})^2} \tag{8.2}$$

$$\delta\sigma = \sqrt{(\delta\sigma_{con})^2 - (\delta\sigma_{fix})^2} \tag{8.3}$$

The effects of most of the systematic uncertainties are estimated with the nuisance parameters, except for the flavour composition (F_{ijk}), which were assessed by repeating the fitting with varied F_{ijk} values and comparing with the nominal cases.

8.13 Summary of Results

Table 8.3 and Table 8.4 summarize the results and uncertainties for the b-tagging efficiency and $t\bar{t}$ cross section, respectively.

With the data sample of 35 pb^{-1}, the statistical uncertainty is the dominant uncertainty for both b-tagging efficiency and $t\bar{t}$ cross section measurement. The measured b-tagging efficiency has a 10% total uncertainty and is consistent with the prediction of detector simulations. The measured $t\bar{t}$ cross section is $176 \pm 22(\text{stat.}) \pm 22(\text{syst.}) \pm 6(\text{lumi})$ pb, larger than the NLO theoretical prediction of $164^{+14.4}_{-15.7}$ [22] but within the uncertainty of the measurement.

	ee	$\mu\mu$	$e\mu$	combined
ϵ_b^{MC} (%)	51.6	51.6	51.6	51.6
ϵ_b^{fit} (%)	63.4	54.6	51.1	54.1
Scale Factor ($\epsilon_b^{fit}/\epsilon_b^{MC}$)	1.23	1.06	0.99	1.05
Relative Stat. Uncertainty (%)	18.5	18.5	12.5	9.1
Syst. Uncertainty Source	$\delta\epsilon_b/\epsilon_b$ (%)			
c-tagging eff	0.3	0.2	0.2	0.2
l-tagging eff	0.3	0.3	0.3	0.3
Background normalization				
Z+jets	3.3	8.1	2.7	3.5
diboson	0.6	0.8	0.9	0.7
single top	0.5	0.5	0.5	0.5
fake lepton	1.7	1.4	1.9	1.5
Flavour composition				
Z+heavy flavour fraction	0.3	1.0	0.3	0.4
Generator	0.3	0.5	0.3	0.4
Parton Shower	0.4	0.5	0.4	0.4
JES (MultijetJES Provider)	0.6	0.9	0.5	0.6
ISR/FSR	1.9	1.5	1.3	1.4
Total Systematic	4.3	8.6	3.8	4.3
Stat.+Syst.	19.0	20.4	13.1	10.1

Table 8.3: Summary of systematic and statistical uncertainties for the ϵ_b measurement in the dilepton channel.

	ee	$\mu\mu$	$e\mu$	combined
$\sigma_{t\bar{t}}$ (pb)	196.4	197.2	162.2	175.6
Relative Stat. Uncertainty (%)	+31.7/-26.7	+25.0/-22.0	+16.8/-15.3	12.5
Syst. Uncertainty Source	$\delta\sigma_{tt}/\sigma_{tt}$ (%)			
Signal Acceptance	+13.1/-10.9	+8.8/-6.2	+8.0/-7.0	+10.5/-9.1
Background rates				
Z+jets background	4.6	8.9	2.9	4.6
dibosn	1.1	1.3	1.6	1.5
single top	0.9	0.8	0.9	0.9
fake lepton	3.5	2.3	4.3	4.0
c-tagging eff	0.3	0.2	0.2	0.2
l-tagging eff	0.3	0.3	0.3	0.3
Z+heavy flavour fraction	0.5	1.1	0.8	0.8
Flavour composition (F_{ijk})	1.6	1.3	1.3	1.4
All Systematic (without Lumi)	+14.5/-12.5	+12.9/-11.3	+9.8/-9.0	+12.4/-11.2
Luminosity	3.4	3.4	3.4	3.4
Stat.+Syst.+Lumi	+35.0/-29.7	+28.3/-25.0	+19.7/-18.1	+17.9/-17.1

Table 8.4: Summary of systematic and statistical uncertainties for the $t\bar{t}$ cross section measurement from the simultaneous fit. The b-tagging working point used here is the SV0 tagging algorithm at weight cut 5.85. The uncertainties on the flavour composition are broken down in to various sources and explained in the text.

Chapter 9

Conclusions and Outlook

The results for the cross section measurement made with a data sample of 35 pb^{-1} are dominated by statistical unertainties. They are

$$\sigma(p+p \to t\bar{t}+X) = [196^{+62}_{-52}(\text{stat.})^{+28}_{-25}(\text{syst.}) \pm 7(\text{lumi.}) \ ] \text{ pb},$$

$$\sigma(p+p \to t\bar{t}+X) = [197^{+49}_{-43}(\text{stat.})^{+25}_{-22}(\text{syst.}) \pm 7(\text{lumi.}) \ ] \text{ pb},$$

and

$$\sigma(p+p \to t\bar{t}+X) = [162^{+27}_{-25}(\text{stat.})^{+16}_{-15}(\text{syst.}) \pm 6(\text{lumi.}) \ ] \text{ pb},$$

in the ee, $\mu\mu$, and $e\mu$ channel, respectively. We combine these measurements together, taking into account correlated uncertainties, and obtain

$$\sigma(p+p \to t\bar{t}+X) = [176 \pm 22(\text{stat.}) \pm 22(\text{syst.}) \pm 6(\text{lumi.}) \ ] \text{ pb}.$$

The $t\bar{t}$ cross section measurement presented in this dissertation has been compared to NNLO theoretical predictions and cross-checked with other techniques presented in [68]. Figure 9.1 summarizes the $t\bar{t}$ cross section measurements and compares the results with theoretical predictions [68]. These measurements are in very good agreement with the

expected results from SM $t\bar{t}$ production predictions. We note that these measurements are strongly correlated as they are based on the same data sample.

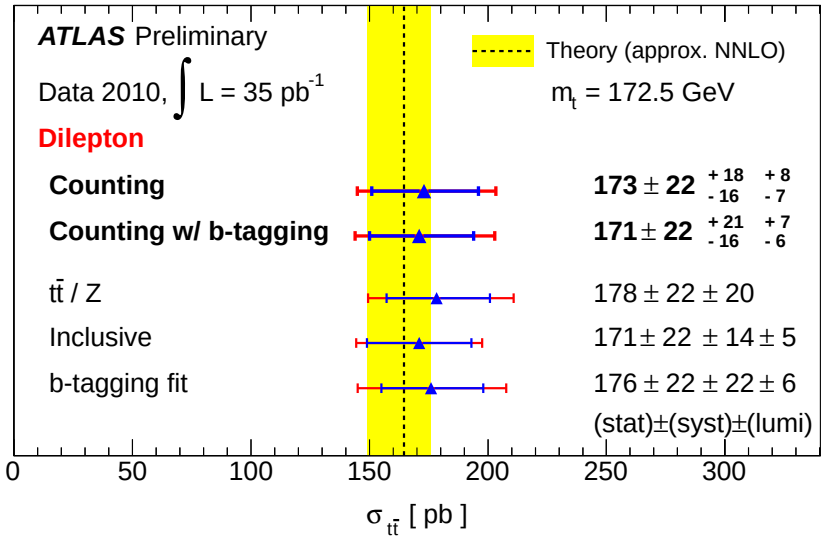

Figure 9.1: The $\sigma_{t\bar{t}}$ cross section measurements presented in the thesis compared to other approaches. The measurement labeled as "b-tagging fit" is the result from this thesis. The yellow bar reflects the uncertainty on the theoretical prediction, which includes some of the NNLO corrections supplemented by soft gluon resummation at the next-to-next-to-leading-logarithm accuracy.

In addition to the $t\bar{t}$ cross section measurement, this thesis also developed a new technique to measure b-tagging efficiency using $t\bar{t}$ events. The measured b-tagging efficiency for the SV0 tagging algorithm is consistent with the prediction by detector simulation. With 35 pb^{-1} of integrated luminosity, the statistical uncertainty is the dominate uncertainty in the b-tagging efficiency measurement. The statistical uncertainty of the b-tagging efficiency as a function of integrated luminosity is shown in Figure 9.2. The statistical uncertainty decreases as the square root of the integrated luminosity. With more than 100 pb^{-1} of integrated luminosity, the b-tagging efficiency uncertainty will be dominated by systematic uncertainties. The b-tagging efficiency can be measured with a precision of about 5% with the tag counting method presented in this dissertation.

Similar techniques can be applied to the $t\bar{t}$ lepton+jets channel [69]. Combining the lepton+jets channel with the dilepton channel will increase the acceptance of $t\bar{t}$ events and

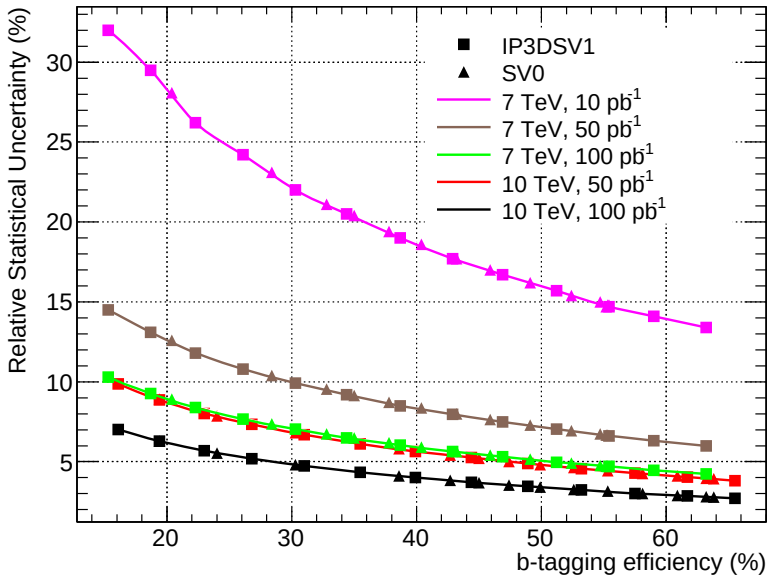

Figure 9.2: Relative statistical uncertainty as a function of b-tagging efficiency and integrated luminosity.

thus further reduce the statistical uncertainty of the b-tagging efficiency measurement. In addition, because of the larger c-jet fraction in the lepton+jets channel, it is also possible to make a first data driven measurement of c-tagging efficiency in ATLAS using the tag counting technique.

The analysis described in this thesis is one of the first measurements of b-tagging efficiency using $t\bar{t}$ events. The conventional methods to measure the b-tagging efficiency are based on a sample of jets containing muons. ATLAS has applied two such methods to the 2010 dataset [70]. The p_T^{rel} method uses templates of the muon momentum transverse to the jet axis to fit the fraction of b-jets before and after b-tagging to extract the b-tagging efficiency. The $D^*\mu$ method explicitly reconstructs the $b \to X\mu D^* \to X\mu D^0$ decay to obtain a pure sample of b-jets to which the b-tagging algorithm is applied.

Even though the various methods all measure the b-tagging efficiency, there are important differences between them. First of all, these methods are affected by different systematics uncertainties. The p_T^{rel} method is sensitive to the Monte Carlo modeling of

the p_T^{rel} templates and the $D^*\mu$ method is mainly affected by the contamination of charm quarks, while the dominate systematic uncertainties in the method described in this analysis are the estimation of Drell-Yan background and the modeling of ISR and FSR. Furthermore, the methods probe a different sample of b-jets: The p_T^{rel} and $D^*\mu$ methods measure the b-tag efficiency in a sample of semileptonic b-jets, while the $t\bar{t}$ based methods measure the b-jets from top quark decay.

The environment of large jet multiplicity in $t\bar{t}$ events is very close to those of the physics samples to which b-tagging is needed. One example of such a physics analysis is the search for the Higgs boson in association with $t\bar{t}$ pairs [71], where at least 6 jets are required in the final state. Another advantage of using $t\bar{t}$ events to measure b-tagging efficiency is the potential of probing high p_T b-jets. Many physics analyses relies on identifying high p_T b-jets. For instance, the Supersymmetry search with b-jets final states requires tagging a b-jets with p_T greater than 100 GeV [72]. The measurement of b-tagging efficiency at such high p_T is challenging with the conventional methods using jet samples, because of the low statistics of high p_T b-jet production in dijet events and the limitation of separating b-jets and light jets using the p_T^{rel} templates [73]. The methods based on $t\bar{t}$ events are not limited by these effects and will be crucial to measure the b-tagging efficiency in the high p_T region.

Bibliography

[1] S.Weinberg, Phys. Rev. Lett. **19**, 1264 (1967).

[2] S. J. Goldstron, A. Salam, Phys. Rev. Lett. **127**, 965 (1962).

[3] S.Glashow, Nucl. Phys. **22**, 579 (1961).

[4] M.Cacciari *et al.*, J. High Energy Phys. **0404**, 068 (2004).

[5] G. Aad *et al.* (ATLAS Collaboration), *Expected performance of the ATLAS experiment: detector, trigger and physics*, no. CERN-OPEN-2008-020 (CERN, Geneva, 2009).

[6] M.Gell-Mann, Phys. Lett. **8**, 214 (1964).

[7] G. Zweig, *An SU_3 model for strong interaction symmetry and its breaking; Part I*, Tech. Rep. CERN-TH-401 (1964).

[8] J.-E. Augustin *et al.*, Phys. Rev. Lett. **33**, 1406 (1974).

[9] J. Aubert *et al.*, Phys. Rev. Lett. **33**, 1404 (1974).

[10] Behrends *et al.* (CLEO Collaboration), Phys. Rev. Lett. **50**, 881 (1983).

[11] M.Kobayashi and T.Maskawa, Progress of Theoretical Physics **49**, 652 (1973).

[12] F.Abe *et al.* (CDF Collaboration), Phys. Rev. Lett. **74**, 2626 (1995).

[13] S.Abashi *et al.* (D0 Collaboration), Phys. Rev. Lett. **74**, 2632 (1995).

[14] M.L.Perl *et al.*, Phys. Rev. Lett. **35**, 22 (1975).

[15] C. Cowan, Jr. *et al.*, Science **124**, 3212 (1956).

[16] G.Arnison *et al.* (UA1 Collaboration), Phys. Lett. **B122**, 103 (1983).

[17] G.Arnison *et al.* (UA1 Collaboration), Phys. Lett. **B126**, 298 (1983).

[18] P. Higgs, Phys. Rev. Lett. **13**, 508 (1964).

[19] B.Carithers and P.Grannis, Beam Line (SLAC) **25(3)**, 4 (1995).

[20] I.Adachi *et al.*, Phys. Rev. Lett. **60**, 97 (1988).

[21] T.Aaltonen *et al.* (CDF Collaboration), Phys. Rev. **D78**, 111101 (2008).

[22] S.Moch and P.Uwer, Phys. Rev. **D78**, 034003 (2008).

[23] G.Aad *et al.* (ATLAS Collaboration), *A combined measurement of the top quark pair production using dilepton and single-lepton final states.*, Tech. Rep. ATLAS-CONF-2011-040 (2011).

[24] S. Frixione *et al.*, JHEP **03**, 092 (2006).

[25] V. M. Abazov *et al.* (D0 Collaboration), Phys. Rev. Lett. **103**, 092001 (2009).

[26] T. Aaltonen *et al.* (CDF Collaboration), Phys. Rev. Lett. **103**, 092002 (2009).

[27] K.Nakamura *et al.* (Particle Data Group), J. Phys. G **37**, 075021 (2010).

[28] T. Aaltonen *et al.* (CDF Collaboration), Tech. Rep. CDF note 9913 (2009).

[29] C. Hill and S. Parke, Phys. Rev. **D 49**, 4454 (1994).

[30] G. Aad *et al.* (ATLAS Collaboration), [5], p. 1514.

[31] G. Aad. *et al.* (ATLAS Collaboration), EPJC **71**, 1577 (2011).

[32] V. Khachatryan. *et al.* (CMS Collaboration), Phys. Lett. **B695**, 424 (2011).

[33] G.Aad *et al.* (ATLAS Collaboration), JINST **3**, S08003 (2008).

[34] G.Aad *et al.* (ATLAS Collaboration), *The ATLAS Computing Model*, Tech. Rep. ATL-SOFT-2004-007 (2005).

[35] G.Aad *et al.* (ATLAS Collaboration), EPJC **71**, 1630 (2011).

[36] G.Aad *et al.* (ATLAS Collaboration), *Updated Luminosity Determination in pp Collisions at* $\sqrt{s} = 7$ *TeV using the ATLAS Detector*, Tech. Rep. ATLAS-CONF-2011-011 (2011).

[37] S. Agostinelli *et al.* (GEANT4 Collaboration), Nucl. Instrum. Meth. **A506**, 250 (2003).

[38] G. Aad *et al.* (ATLAS Collaboration), Eur. Phys. J. **C70**, 823 (2010).

[39] S. Frixione, P. Nason, and B. R. Webber, JHEP **08**, 007 (2003).

[40] P. Nadolsky *et al.*, Phys. Rev. **D78**, 013004 (2008).

[41] M. Aliev *et al.*, Comput. Phys. Commun. **182**, 1034 (2011).

[42] S. Frixione *et al.*, JHEP **07**, 029 (2008).

[43] M. Mangano *et al.*, JHEP **0307**, 001 (2003).

[44] J. Pumplin *et al.*, JHEP **07**, 012 (2002).

[45] N. Benekos *et al.*, *Lepton trigger and identification for the Winter 2011 top quark analyses*, Tech. Rep. ATL-COM-PHYS-2011-123 (2011).

[46] M. Cacciari, G. P. Salam, and G. Soyez, JHEP **04**, 063 (2008).

[47] L. Asquith *et al.* (ATLAS Collaboration), *Performance of Jet Algorithms in the ATLAS Detector*, Tech. Rep. ATL-COM-PHYS-2009-630 (2009).

[48] J. F. Arguin *et al.* (ATLAS Collaboration), *Jet selection for top physics*, Tech. Rep. ATL-COM-PHYS-2010-835 (2010).

[49] G.Aad *et al.* (ATLAS Collaboration), *Data-Quality Requirements and Event Cleaning for Jets and Missing Transverse Energy Reconstruction with the ATLAS Detector in Proton-Proton Collisions at a Center-of-Mass Energy of* $\sqrt{s} = 7$ *TeV*, Tech. Rep. ATL-CONF-2010-038 (2010).

[50] J.Almond *et al.* (ATLAS Collaboration), *The measurement of* $t\bar{t}$ *cross section in the dilepton decay channel with cut-and-count methods at 7 TeV with 35.3* pb^{-1}, Tech. Rep. ATL-PHYS-INT-2011-046 (2011).

[51] *Analysis of* $t\bar{t}$ *production in the dilepton decay channel at* 7 TeV *with* 2.9 pb^{-1}, Tech. Rep. ATL-COM-PHYS-2010-856 (2010).

[52] G. Aad *et al.* (ATLAS Collaboration), [5], p. 397.

[53] S. S. B. Heinemann, F. Hirsch (ATLAS Collaboration), *Performance of the ATLAS Secondary Vertex b-tagging Algorithm in 7 TeV Collision Data*, Tech. Rep. ATL-COM-PHYS-2010-274 (2010).

[54] G. Aad *et al.* (ATLAS Collaboration), [5], p. 504.

[55] S. Frixione *et al.*, JHEP **09**, 126 (2007).

[56] A. Martin *et al.*, Eur. Phys. J. **C63**, 189 (2009).

[57] R. Ball *et al.*, Nucl. Phys. **B838**, 136 (2010).

[58] G. Aad *et al.* (ATLAS Collaboration), [5], p. 874.

[59] B. P. Kersevan and E. Richter-Was (2004), arXiv:hep-ph/0405.247.

[60] S. Allwood-Spires *et al.* (ATLAS), *Monte Carlo samples used for top physics: Top Working Group Note IX*, Tech. Rep. ATL-COM-PHYS-2010-836 (2010).

[61] G.Aad *et al.* (ATLAS Collaboration), Eur. Phys. J. C **71**, 1512 (2010).

[62] S. Cabreran Urban *et al.* (ATLAS Collaboration), *Jets, Missing Transverse Energy and Taus for Top Physics Analyses in Release 16 with the 2010 Dataset*, Tech. Rep. ATL-COM-PHYS-2011-132 (2011).

[63] G.Aad *et al.* (ATLAS Collaboration), *ATLAS Jet energy resolution and reconstruction efficiencies from in-situ techniques with the ATLAS Detector Using Proton-Proton Collisions at a Center of Mass Energy* $\sqrt(s) = 7$ TeV, Tech. Rep. ATLAS-CONF-2010-054 (2010).

[64] J. M. Campbell *et al.*, Phys. Rev. **D70**, 094012 (2004).

[65] N. Kidonakis, PoS **DIS2010**, 196 (2010).

[66] J. Butterworth *et al.*, *Single Boson and Diboson Production Cross Sections in pp Collisions at sqrt(s)=7 TeV*, Tech. Rep. ATL-COM-PHYS-2010-695 (2010).

[67] G. Aad *et al.* (ATLAS Collaboration), [5], p. 534.

[68] G.Aad *et al.* (ATLAS Collaboration), *Measurement of the top quark pair production cross-section with ATLAS in pp collisions at* $\sqrt{s} = 7$ *TeV in dilepton final states*, Tech. Rep. ATLAS-CONF-2011-034 (2011).

[69] B. Alvarez *et al.* (ATLAS Collaboration), *b-jet Tagging for Top Physics: Perfomance studies, Calibrations and Heavy Flavor Fractions*, Tech. Rep. ATL-COM-PHYS-2011-124 (2011).

[70] G.Aad *et al.* (ATLAS Collaboration), *Calibrating the b-Tag Efficiency and Mistag Rate in 35* pb^{-1} *of Data with the ATLAS Detector*, Tech. Rep. ATLAS-CONF-2011-089 (2011).

[71] G. Aad *et al.* (ATLAS Collaboration), [5], p. 1333.

[72] G. Aad *et al.* (ATLAS Collaboration), [5], p. 1606.

[73] G. Aad *et al.* (ATLAS Collaboration), [5], p. 534.

Appendix A

Results with Other b-tagging Algorithms

Section 8.13 summarized the b-tagging efficiency and $t\bar{t}$ cross section measurement using "SV0" at 50% working point.

In this analysis, other tagging algorithms and working points were also studied, and the fitting results of the b-tagging efficiency and $t\bar{t}$ cross section at various working points are summarized in Table A.1. The measured b-tagging efficiencies are consistent with MC simulations. With the available amount of data, the statistical uncertainty is still the dominates uncertainty in the b-tagging efficiency measurement.

Tagging Algorithm	SV0	JetProb	JetProb	IP3DSV1	JetFitterComb.
Working Point	5.85	3.25	2.05	4.50	2.00
ϵ_b^{MC}	51.6	52.2	72.1	61.8	61.8
ϵ_b^{fit}	54.1	56.7	78.8	66.1	66.6
Scale Factor ($\epsilon_b^{fit}/\epsilon_b^{MC}$)	1.05	1.09	1.09	1.07	1.07
Relative Stat. Uncertainty	9.1	8.8	6.1	7.2	7.1
Systematic Uncertainties	$\delta\epsilon_b/\epsilon_b$ (%)				
c-tagging Uncertainty	0.2	0.2	0.6	0.2	0.2
Light Jet Rejection	0.3	0.5	0.9	0.1	0.1
Background Normalization					
Z+Jets	3.5	3.6	2.7	2.8	2.8
Diboson	0.7	0.8	0.7	0.8	0.8
single top	0.5	0.5	0.4	0.5	0.6
fake lepton	1.5	1.3	1.0	1.1	1.1
Z+heavy flavor fraction	0.4	0.4	0.3	0.2	0.2
Flavor composition (F_{ijk})	1.6	1.8	1.9	1.6	1.7
Syst. Uncertainty	4.3	4.4	3.7	3.6	3.6
Stat.+Syst.	10.1	9.8	7.1	8.0	8.0
σ^{tt} (pb)	175.3	173.2	174.6	178.5	179.2
Relative Stat. Uncertainty (%)	12.5	12.6	12.3	12.2	12.1
Syst. Uncertainty Source	$\delta\sigma_{tt}/\sigma_{tt}$ (%)				
Signal Acceptance	+10.5/-9.1	+10.5/-9.1	+10.5/-9.1	+10.5/-9.1	+10.5/-9.1
Background Normalization					
Z+Jets	4.6	4.6	3.9	4.2	4.2
Diboson	1.5	1.5	1.3	1.3	1.3
Single top	0.9	0.9	0.7	0.8	0.7
Fake lepton	4.0	4.2	3.7	3.2	3.2
c-tagging Uncertainty	0.2	0.2	0.5	0.1	0.1
Light Jet Rejection	0.3	0.4	0.7	0.1	0.2
Z+heavy flavor fraction	0.8	0.8	0.7	0.5	0.7
Flavor composition (F_{ijk})	1.4	1.5	1.6	1.2	1.3
Syst. Uncertainty (without Lumi.)	+12.4/-11.2	+12.5/-11.3	+12.0/-10.8	+11.9/-10.7	+11.9/-10.7
Luminosity Uncertainty	3.4	3.4	3.4	3.4	3.4
Total Uncertainty	17.9/-17.1	+18.1/-17.3	+17.5/-16.7	+17.4/-16.6	+17.3/-16.5

Table A.1: Measured b-tagging efficiency and $t\bar{t}$ cross section at various b-tagging working points and the expected uncertainties when combining ee, $\mu\mu$, and $e\mu$ channels. The break down of systmeatic uncertainties for individual channels are shown in Table 8.3 and Table 8.4.

Appendix B

List of MC samples

ID	Description	Matrix Element	Parton Shower	cross section [pb]	k-factor
5200	$t\bar{t}$ No full hadr. (e, μ, τ)	MC@NLO	Herwig	80.107	1.12
8340	tchan $\rightarrow e$	MC@NLO	Herwig	7.152	1
8341	tchan $\rightarrow \mu$	MC@NLO	Herwig	7.176	1
8342	tchan $\rightarrow \tau$	MC@NLO	Herwig	7.128	1
8343	schan $\rightarrow e$	MC@NLO	Herwig	0.4685	1
8344	schan $\rightarrow \mu$	MC@NLO	Herwig	0.4684	1
8345	schan $\rightarrow \tau$	MC@NLO	Herwig	0.4700	1
8346	$Wt \rightarrow$ inclusive	MC@NLO	Herwig	14.581	1

Table B.1: Top Monte-Carlo samples.

ID	Description	Matrix Element	Parton Shower	cross section [pb]	k-factor
7680	Wenu Np0	Alpgen	Herwig	6913.3	1.2
7681	Wenu Np1	Alpgen	Herwig	1293.0	1.2
7682	Wenu Np2	Alpgen	Herwig	377.1	1.2
7683	Wenu Np3	Alpgen	Herwig	100.9	1.2
7684	Wenu Np4	Alpgen	Herwig	25.3	1.2
7685	Wenu Np5	Alpgen	Herwig	6.9	1.2
7690	Wmunu Np0	Alpgen	Herwig	6935.4	1.2
7691	Wmunu Np1	Alpgen	Herwig	1281.2	1.2
7692	Wmunu Np2	Alpgen	Herwig	375.3	1.2
7693	Wmunu Np3	Alpgen	Herwig	101.1	1.2
7694	Wmunu Np4	Alpgen	Herwig	25.7	1.2
7695	Wmunu Np5	Alpgen	Herwig	7.0	1.2
7700	Wtaunu Np0	Alpgen	Herwig	6835.8	1.2
7701	Wtaunu Np1	Alpgen	Herwig	1276.8	1.2
7702	Wtaunu Np2	Alpgen	Herwig	376.6	1.2
7703	Wtaunu Np3	Alpgen	Herwig	100.8	1.2
7704	Wtaunu Np4	Alpgen	Herwig	25.7	1.2
7705	Wtaunu Np5	Alpgen	Herwig	7.0	1.2

Table B.2: W+jets samples.

ID	Description	Matrix Element	Parton Shower	cross section [pb]	k-factor
7650	Zee Np0	Alpgen	Herwig	661.9	1.25
7651	Zee Np1	Alpgen	Herwig	133.3	1.25
7652	Zee Np2	Alpgen	Herwig	40.3	1.25
7653	Zee Np3	Alpgen	Herwig	11.2	1.25
7654	Zee Np4	Alpgen	Herwig	2.7	1.25
7655	Zee Np5	Alpgen	Herwig	0.8	1.25
7660	Zmumu Np0	Alpgen	Herwig	657.7	1.25
7661	Zmumu Np1	Alpgen	Herwig	132.8	1.25
7662	Zmumu Np2	Alpgen	Herwig	39.6	1.25
7663	Zmumu Np3	Alpgen	Herwig	11.1	1.25
7664	Zmumu Np4	Alpgen	Herwig	2.8	1.25
7665	Zmumu Np5	Alpgen	Herwig	0.8	1.25
7670	Ztautau Np0	Alpgen	Herwig	657.4	1.25
7671	Ztautau Np1	Alpgen	Herwig	133.0	1.25
7672	Ztautau Np2	Alpgen	Herwig	40.4	1.25
7673	Ztautau Np3	Alpgen	Herwig	11.0	1.25
7674	Ztautau Np4	Alpgen	Herwig	2.9	1.25
7675	Ztautau Np5	Alpgen	Herwig	0.7	1.25

Table B.3: Z+jets/Drell-Yan samples with phase space cuts $m_{l^+l^-} > 40$ GeV.

ID	Description	Matrix Element	Parton Shower	cross section [pb]	k-factor
116250	Zee Np0	Alpgen	Herwig	3054.7	1.25
116251	Zee Np1	Alpgen	Herwig	84.910	1.25
116252	Zee Np2	Alpgen	Herwig	41.188	1.25
116253	Zee Np3	Alpgen	Herwig	8.3498	1.25
116254	Zee Np4	Alpgen	Herwig	1.8535	1.25
116255	Zee Np5	Alpgen	Herwig	0.46128	1.25
116260	Zmumu Np0	Alpgen	Herwig	3054.9	1.25
116261	Zmumu Np1	Alpgen	Herwig	84.778	1.25
116262	Zmumu Np2	Alpgen	Herwig	41.13	1.25
116263	Zmumu Np3	Alpgen	Herwig	8.3441	1.25
116264	Zmumu Np4	Alpgen	Herwig	1.8652	1.25
116265	Zmumu Np5	Alpgen	Herwig	0.45995	1.25
116270	Ztautau Np0	Alpgen	Herwig	3054.8	1.25
116271	Ztautau Np1	Alpgen	Herwig	84.882	1.25
116272	Ztautau Np2	Alpgen	Herwig	41.275	1.25
116273	Ztautau Np3	Alpgen	Herwig	8.3473	1.25
116274	Ztautau Np4	Alpgen	Herwig	1.8298	1.25
116275	Ztautau Np5	Alpgen	Herwig	0.46316	1.25

Table B.4: Low mass Z+jets/Drell-Yan samples with 10 GeV $< m_{l^+l^-} <$ 40 GeV.

ID	Description	Matrix Element	Parton Shower	cross section [pb]	k-factor
6280	WbbNp0	Alpgen	Herwig	3.2	1.2
6281	WbbNp1	Alpgen	Herwig	2.6	1.2
6282	WbbNp2	Alpgen	Herwig	1.4	1.2
6283	WbbNp3	Alpgen	Herwig	0.6	1.2

Table B.5: W+bb samples.

ID	Description	Matrix Element	Parton Shower	cross section [pb]	k-factor
9300	Z+bb Np0	Alpgen	Herwig	6.52	1.25
9301	Z+bb Np1	Alpgen	Herwig	2.47	1.25
9302	Z+bb Np2	Alpgen	Herwig	0.808	1.25
9303	Z+bb Np3	Alpgen	Herwig	0.387	1.25
9305	Z+bb Np0	Alpgen	Herwig	6.52	1.25
9306	Z+bb Np1	Alpgen	Herwig	2.47	1.25
9307	Z+bb Np2	Alpgen	Herwig	0.808	1.25
9308	Z+bb Np3	Alpgen	Herwig	0.387	1.25
9310	Z+bb Np0	Alpgen	Herwig	6.52	1.25
9311	Z+bb Np1	Alpgen	Herwig	2.47	1.25
9312	Z+bb Np2	Alpgen	Herwig	0.808	1.25
9313	Z+bb Np3	Alpgen	Herwig	0.387	1.25

Table B.6: Z+bb samples.

ID	Description	Matrix Element	Parton Shower	cross section [pb]	k-factor
7100	WW + 0j	Alpgen	Herwig	2.049	1.21
7101	WW + 1j	Alpgen	Herwig	0.987	1.21
7102	WW + 2j	Alpgen	Herwig	0.441	1.21
7103	WW + 3j	Alpgen	Herwig	0.178	1.21
7104	WZ + 0j	Alpgen	Herwig	0.664	1.21
7102	WW + 2j	Alpgen	Herwig	0.441	1.21
7106	WZ + 2j	Alpgen	Herwig	0.221	1.21
7107	WZ + 3j	Alpgen	Herwig	0.093	1.21
7108	ZZ + 0j	Alpgen	Herwig	0.494	1.21
7109	ZZ + 1j	Alpgen	Herwig	0.225	1.21
7110	ZZ + 2j	Alpgen	Herwig	0.088	1.21
7111	ZZ + 3j	Alpgen	Herwig	0.028	1.21

Table B.7: Diboson samples.

ID	Description	Matrix Element	Parton Shower	cross section [pb]	k-factor
5205	$t\bar{t}$	AcerMC	Pythia	58.23	1.53
5860	$t\bar{t}$	POWHEG	Herwig	79.118	1.13
5861	$t\bar{t}$	POWHEG	Pythia	79.118	1.13
117255	$t\bar{t}$ ISR min	AcerMC	Pythia	58.23	1.53
117256	$t\bar{t}$ ISR max	AcerMC	Pythia	58.23	1.53
117257	$t\bar{t}$ FSR min	AcerMC	Pythia	58.23	1.53
117258	$t\bar{t}$ FSR max	AcerMC	Pythia	58.23	1.53

Table B.8: Systematic generator and ISR/FSR samples.

ID	Description	Matrix Element	Parton Shower	cross section (NNLO) [pb]
106087	$Z \to ee$	MC@NLO	Herwig	989
106088	$Z \to \mu\mu$	MC@NLO	Herwig	989

Table B.9: Samples used for inclusive Z analysis.